POLITECNICO DI TORINO
Repository ISTITUZIONALE

On Anatomical Prior Kernel Distortion for Tomographic Microwave Imaging Stroke Monitoring

Original
On Anatomical Prior Kernel Distortion for Tomographic Microwave Imaging Stroke Monitoring / Masaquiza Caiza, A.R., Rodríguez-Duarte, D.O., Gugliermino, M., Mariano, V., Vipiana, F.. - In: IEEE OPEN JOURNAL OF ANTENNAS AND PROPAGATION. - ISSN 2637-6431. - (2026). [10.1109/ojap.2026.3724057]

Availability:
This version is available at: 11583/3015269 since: 2026-09-13T08:41:39Z

Publisher:
IEEE

Published
DOI:10.1109/ojap.2026.3724057

Terms of use:

This article is made available under terms and conditions as specified in the corresponding bibliographic description in the repository

Publisher copyright
IEEE postprint/Author's Accepted Manuscript

©2026 IEEE. Personal use of this material is permitted. Permission from IEEE must be obtained for all other uses, in any current or future media, including reprinting/republishing this material for advertising or promotional purposes, creating new collecting works, for resale or lists, or reuse of any copyrighted component of this work in other works.

(Article begins on next page)

26 November 2026

This article has been accepted for publication in IEEE Open Journal of Antennas and Propagation. This is the author's version which has not been fully edited and content may change prior to final publication. Citation information: DOI 10.1109/OJAP.2026.3724057

IEEE Open Journal of Antennas and Propagation

Received XX Month, XXXX; revised XX Month, XXXX; accepted XX Month, XXXX; Date of publication XX Month, XXXX; date of current version XX Month, XXXX.

Digital Object Identifier 10.1109/OJAP.2020.1234567

On Anatomical Prior Kernel Distortion for Tomographic Microwave Imaging Stroke Monitoring

A. RAMIRO MASAQUIZA-CAIZA (Graduate Student Member, IEEE), DAVID O. RODRIGUEZ-DUARTE (Member, IEEE), MARTINA GUGLIERMINO (Graduate Student Member, IEEE), VALERIA MARIANO, AND FRANCESCA VIPIANA, (Senior Member, IEEE)

[1]Department of Electronics and Telecommunications, Politecnico di Torino, 10129 Torino, Italy

CORRESPONDING AUTHORS: FRANCESCA VIPIANA AND DAVID O. RODRIGUEZ-DUARTE (e-mail:francesca.vipiana@polito.it; david.rodriguez@polito.it)

This work was supported in part by the research project "MedWaveImage", funded by Interreg Central Europe (CE0200670), and by the research project "3BAtwin" funded by the Horizon EU FP (101159623).

ABSTRACT This paper investigates the role of prior internal structural, morphological, and dielectric information in constructing linearized inversion kernels for microwave imaging-based brain stroke monitoring, with emphasis on structural-model mismatch and regularization effects. Although detailed anatomical models are often assumed to improve reconstruction accuracy, their availability, reliability, and practical integration remain limited in realistic clinical scenarios. A systematic methodological framework is therefore adopted to assess how the inclusion, simplification, or absence of morphological information affects the performance of the inversion kernels constructed under the Born approximation and regularized using the truncated singular value decomposition. A multi-patient numerical study is used to capture anatomical variability and evaluate inversion operators with progressively reduced structural complexity, ranging from multi-tissue representations to homogeneous models. Stroke evolution, including both hemorrhagic and ischemic cases, is simulated and analyzed under varying spatial-resolution, lesion-morphology, and lesion-location conditions. In addition, this work first harmonizes the terminology and definitions of imaging metrics commonly used in recent microwave medical imaging literature, providing a consistent framework for their interpretation and cross-study comparison, and second proposes a unified statistically based metric, referred to as the Spearman-weighted metric, providing a global score that enables direct and consistent comparison across inversion kernels. The results indicate that reconstruction quality is only weakly dependent on the level of structural detail embedded in the inversion kernel. In many cases, simplified models are sufficient to capture the main features of stroke evolution, suggesting that highly detailed patient-specific information may not be strictly necessary for monitoring-oriented applications. Overall, the proposed framework provides a general methodological basis for evaluating structural-model mismatch in inversion kernels and supports the use of reduced-complexity inversion strategies when accurate prior information is unavailable.

INDEX TERMS A priori information, Born approximation, brain stroke monitoring, inverse scattering, inversion kernels, microwave imaging, simplified model, truncated singular value decomposition.

I. INTRODUCTION

MEDICAL microwave imaging (MMWI) is a centimetric-resolution diagnostic and monitoring technique that exploits the frequency-dependent dielectric contrast between biological tissues and pathophysiological alterations at microwaves to generate images in a non-ionizing, non-invasive, potentially real-time, and continuous manner [1]. Hence, it might serve as a complementary

This work is licensed under a Creative Commons Attribution 4.0 License. For more information, see https://creativecommons.org/licenses/by/4.0/

This work is licensed under a Creative Commons Attribution-NonCommercial-NoDerivatives 4.0 License.
For more information, see https://creativecommons.org/licenses/by-nc-nd/4.0/

This article has been accepted for publication in IEEE Open Journal of Antennas and Propagation. This is the author's version which has not been fully edited and content may change prior to final publication. Citation information: DOI 10.1109/OJAP.2026.3724057

neuroimaging modality to current gold standards, including magnetic resonance imaging (MRI), computed tomography (CT), X-ray, and positron emission tomography (PET), which are costly, bulky and even harmful in the case of the later three [2], [3], and have limited applicability in the case of stoke monitoring.

Stroke is a highly prevalent and severe neurological condition characterized by a sudden disruption of oxygen-rich blood flow to the brain, leading to impaired or transient neurological function. In the acute phase, stroke evolves as a highly dynamic and patient-specific pathology, with neuronal loss occurring at a rate of millions of cells per minute. Two main types are distinguished: intracerebral hemorrhage (ICH), which accounts for a smaller fraction of cases but is associated with higher mortality, and acute ischemic stroke (AIS), which is more frequent and caused by vascular occlusion. The stroke prognosis critically depends on prompt intervention within the first hours after onset, encompassing rapid diagnosis, treatment administration, and continuous monitoring. This time-sensitive intervention is essential to improve clinical outcomes and reduce the risk of long-term disability, functional deficits, or even death.

From an electromagnetic (EM) perspective, stroke monitoring involves tracking a clinically fast, time-variant, concentrated dielectric contrast within a non-accessible, highly complex, multi-layer, lossy, and dispersive domain. MMWI estimates this dielectric contrast by solving an ill-posed, ill-conditioned, and nonlinear inverse-scattering problem [4]–[6]. In this process, a limited number of scattered-field samples are collected outside the domain of imaging (DoI), which, in this work, corresponds to the head. These measurements are then mapped through an inversion or imaging kernel to generate scan-like images. Consequently, if the kernel is not sufficiently representative of the actual scenario, the resulting modeling errors may propagate into the reconstruction and degrade image quality.

The introduction of *a priori* anatomical information—such as morphological features, including shapes, structures, dimensions, boundaries, discontinuities, and/or dielectric distributions—serves as a regularizing and potentially enhancing element. In medical applications, several studies have explored incorporating such prior information by leveraging complementary imaging modalities, including MRI, CT, and ultrasound (US). In the context of breast imaging, [7] introduces a soft-prior regularization framework that integrates MRI-segmented anatomical regions into the inverse problem without enforcing exact EM properties within each tissue class, thereby improving the reconstructions. The work in [8] uses a delay-and-sum US beamforming algorithm to obtain maps, which are then segmented via k-means clustering to generate an inhomogeneous numerical model of the DoI. This anomically-informed background is then used with an EM finite element method (FEM)-based model that supports a contrast source inversion (CSI) method to generate quantitative reconstructions. Similarly, [9], [10] demonstrated that patient-specific structural maps, acquired via radar based techniques, substantially improve reconstruction quality. Meanwhile, in the context of bone imaging, [11] uses prior structural information about different tissues as an inhomogeneous background to assess bone density in an osteoporosis-affected leg, thereby enhancing localization of the tibia and fibula and monitoring changes. In this case, the a priori information is obtained either from MRI with k-means clustering or from a blind FEM-CSI (without a priori information). For stroke, [12] addressed the lack of patient-specific prior knowledge by proposing a two-step method that directly extracts a patient-specific background model from the same measurement data used for diagnosis. Previous studies [11], [12] demonstrated that prior knowledge can be not only extracted from another neuroimaging modality but also retrieved from the microwave measurements themselves.

A broader perspective on prior knowledge, beyond these application-specific contributions, is discussed in [13]. It provides a unified perspective by introducing a space-time-frequency (STF) classification framework for prior knowledge in MMWI, encompassing both quantitative and qualitative algorithms across various imaging applications. The analysis is conducted using the distorted Born iterative method (DBIM) and pulse-radar experiments, and the results show overall performance improvements when accurate prior information is available.

Against this landscape, a fundamental and still open question emerges: what level of accuracy in the a priori anatomical and dielectric information embedded in the inversion kernel is required to achieve meaningful, clinically relevant MMWI outcomes? This is especially relevant in real clinical scenarios, where this information may be inherently limited and distorted [14]. Furthermore, even in an ideal scenario with complete structural information available, the intra-tissue dielectric variability introduces an additional distortion in the inversion kernel. These considerations open the possibility of exploring different clinically motivated inversion kernel configurations from a complete patient-specific multi-tissue model to a simplified homogeneous head model, each motivated by realistic clinical practice. Addressing this question systematically and rigorously requires not only evaluating the degree of prior anatomical information embedded in the inversion kernels, but also consistently assessing the imaging quality.

Quantitative imaging performance metrics are widely used to assess the quality of imaging reconstructions [15]–[19]. However, to the best of our knowledge, the metrics currently used in the literature are evaluated separately and independently, without a homogenized terminology, making cross-study comparisons difficult and sometimes ambiguous, as discussed in [15], [20]. Each metric provides specific information about a particular aspect of the reconstruction quality, such as localization accuracy, shape fidelity, or dielectric property retrieval error. Nevertheless, when redun-

This work is licensed under a Creative Commons Attribution-NonCommercial-NoDerivatives 4.0 License.
For more information, see https://creativecommons.org/licenses/by-nc-nd/4.0/

This article has been accepted for publication in IEEE Open Journal of Antennas and Propagation. This is the author's version which has not been fully edited and content may change prior to final publication. Citation information: DOI 10.1109/OJAP.2026.3724057

dant information is present across different imaging metrics, a statistical average over the metrics may not be the fairest or most balanced approach.

With the end of rigorously and systematically addressing the question of anatomical prior information for stroke monitoring, here we present an extensive multi-subject and multi-variable 2-D numerical study that, first, provides a controlled framework and, second, retains the complexity of the inverse-scattering problem while offering lower computational cost. As variables, it covers stroke and head morphology, stroke placement, intra-tissue permittivity variability, spatial resolution, and number of radiating elements, as well as different signal-to-noise levels and evolving worsening and recovery scenarios, accounting for more than 180,000 brain stroke-monitoring scenarios. As an imaging algorithm, we employ a differential approach and a non-iterative linearized one based on the Born approximation and truncated singular value decomposition (TSVD), previously applied to stroke monitoring in e.g. [21]. Then, to assess the results, we employ feature-specific imaging metrics on both qualitative (normalized contrast maps) and quantitative (complex contrast maps) retrievals, as well as a proposed unified, statistically motivated Spearman-Weighted Metric (SWM).

To summarize, the main contributions of this paper are threefold. First, a systematic evaluation of the impact of the degree of detail in prior anatomical and dielectric information on MMWI reconstruction quality is presented, based on a set of clinically motivated inversion kernel models that account for realistic scenarios in brain stroke monitoring. Second, a homogenization of the terminology and definitions of the imaging metrics used in the recent MMWI literature is proposed, providing a consistent framework for their interpretation and cross-study comparison. Third, a methodology for combining the individual metrics into a single statistically based representative quantity is introduced: the Spearman-weighted metric (SWM). It provides a global quality score for the reconstructed dielectric contrast maps, enabling a direct and consistent evaluation of inversion kernels with different amounts of prior anatomical information. All these contributions aim to provide a practically grounded analysis of the trade-off between the complexity of the inversion kernel and the achievable imaging quality in the clinically relevant scenario of brain stroke microwave monitoring.

The paper is organized as follows. Section II illustrates the problem statement and the imaging performance metrics. Details regarding the numerical framework and the MMWI scenario used to address the assessment are described in Section III. In Section IV, numerical results are discussed, and Section V concludes the paper.

This paper thoroughly expands on the preliminary work presented in [22].

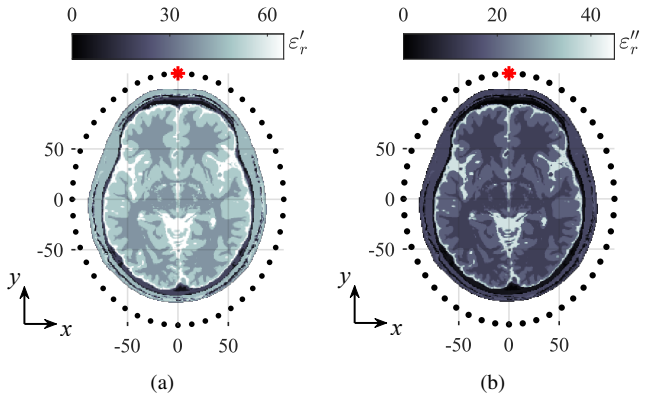

FIGURE 1. Dielectric property maps of an eleven-tissue head model obtained from an MRI slice: (a) real part of ε_r and (b) imaginary part of ε_r. Dimensions are in mm. The 48 points indicate the position of the source-line elements.

II. PROBLEM STATEMENT

A. The inverse scattering problem

A typical brain MMWI scenario is shown in Fig. 1. An antenna array of N_a elements is placed in proximity to the head, coupled to the tissues using a matching medium, and collects the scattered signals to reconstruct the spatial distribution of the complex dielectric properties within the DoI, i.e., the head. Since the scattered data can be collected only within a limited region outside the DoI, the inverse problem is inherently ill-posed, making the estimation of the dielectric properties challenging. Considering a bounded, reciprocal, non-magnetic background ($\mu_b = \mu_0$), with known complex permittivity $\varepsilon_b(\mathbf{r})$ containing a dielectric scatter of unknown complex permittivity, the contrast function at a given instant t_m is defined as $\Delta\varepsilon(\mathbf{r}, t_m) = \varepsilon(\mathbf{r}, t_m) - \varepsilon_b(\mathbf{r})$, where $\mathbf{r}$ is a position vector, μ_b and μ_0 the permeability of the background and free-space, respectively. The scattered field $\mathbf{E}^{\mathrm{sc}}(\mathbf{r}, t_m)$ at any position is defined as in [4], [5]:

$$\mathbf{E}^{\mathrm{sc}}(\mathbf{r}, t_m) = \omega^2 \mu_0 \int_V \Delta\varepsilon(\mathbf{r}', t_m)\, \mathbf{G}_b(\mathbf{r}, \mathbf{r}') \cdot \mathbf{E}^{\mathrm{tot}}(\mathbf{r}', t_m)\, dV', \tag{1}$$

where $\omega = 2\pi f$ is the angular frequency with f the frequency of the excitation, and $\mathbf{G}_b(\mathbf{r}, \mathbf{r}')$ the background Green function. From (1), it is evident that the scattered field depends on both the contrast function and the total field, $\mathbf{E}^{\mathrm{tot}}$, which itself depends on the contrast, making the relationship nonlinear; additionally, $\mathbf{G}_b$ is generally unknown for non-homogeneous or enclosed backgrounds, e.g., the head tissues. The work in [23] derived a model that overcomes this limitation for the case of point-like field sampling, i.e., when the receiver measures the field component $\widehat{\mathbf{p}}_i \cdot \mathbf{E}(\mathbf{r}_i)$ at a discrete location $\mathbf{r}_i$, where $\widehat{\mathbf{p}}_i$ is the polarization of antenna or the field probe. For such cases, $\mathbf{G}_b$, that in general has no-closed form solution in a non-homogeneous media, is replaced by a Green's vector, equivalent to the incident field of the i-th receiver when it transmits, divided by a scalar normalization constant $\mu_b(\mathbf{r}_i) J_i \Delta\Omega_i$, with $J_i \Delta\Omega_i$ the

This work is licensed under a Creative Commons Attribution-NonCommercial-NoDerivatives 4.0 License.
For more information, see https://creativecommons.org/licenses/by-nc-nd/4.0/

This article has been accepted for publication in IEEE Open Journal of Antennas and Propagation. This is the author's version which has not been fully edited and content may change prior to final publication. Citation information: DOI 10.1109/OJAP.2026.3724057

normalizing current element, wherein J_i is its density and $\Delta\Omega_i$ its volume. Thus, the scalar response R_{ik} at port i-th due to excitation at port k-th can be written as:

$$R_{ik}(t_m) = \frac{j\omega}{\mu_b(\mathbf{r}_i) J_i \Delta\Omega_i} \int_V \mu_b(\mathbf{r}') \Delta\varepsilon(\mathbf{r}', t_m)\, \mathbf{E}_i^{\mathrm{inc}}(\mathbf{r}') \cdot \mathbf{E}_k^{\mathrm{tot}}(\mathbf{r}', t_m)\, dV', \tag{2}$$

where $\mathbf{E}_i^{\mathrm{inc}}$ is the field radiated by the i-th port, and $\mu_b(\mathbf{r}_i)$ the permeability at the discrete location $\mathbf{r}_i$. The response $R_{ik}(t_m)$ has units (V/m) and is a discretized measurement of the scattered electric field.

In the 2-D TM case, the volume integral reduces to a surface integral, and $\Delta\Omega_i \to \Delta S_i$, with ΔS_i the area of the normalizing current element $J_i \Delta S_i$. Thus (2) becomes:

$$\mathbf{E}_{ik}^{\mathrm{sc}}(t_m) = \frac{j\omega}{J_i \Delta S_i} \int_S \Delta\varepsilon(\mathbf{r}', t_m)\, \mathbf{E}_i^{\mathrm{inc}}(\mathbf{r}') \cdot \mathbf{E}_k^{\mathrm{tot}}(\mathbf{r}', t_m)\, dS', \tag{3}$$

where $\mathbf{E}_{ik}^{\mathrm{sc}}(t_m)$ is scatter field at t_m. To deal with the nonlinearity of the resulting formulation, approaches based on the Born approximation have proved to be effective when dealing with weak scatterers. In stroke monitoring, its viability depends on the adopted background model, which determines the contrast function of the scattering problem. Moreover, when moving to a differential approach as in [21], [24]–[26], the Born approximation becomes increasingly valid, since ICH or AIS lesions induce localized and magnitude-limited contrast variations. Thus, the first-order Born approximation is applicable, whereby the total field is approximated by the incident field, i.e., $\mathbf{E}_k^{\mathrm{tot}}(\mathbf{r}, t_m) \approx \mathbf{E}_k^{\mathrm{inc}}(\mathbf{r})$. Accordingly, a time-dependent contrast function that represents the spatio-temporal permittivity variation between two consecutive time instants between t_0 and t_1 can be defined as $\Delta\varepsilon(\mathbf{r}, t_0, t_1) = \varepsilon(\mathbf{r}, t_0) - \varepsilon(\mathbf{r}, t_1)$. The resulting differential scattered field due to lesion progression is $\Delta E_{ik}^{\mathrm{sc}} = E_{ik}^{\mathrm{sc}}(t_0) - E_{ik}^{\mathrm{sc}}(t_1)$ and can be expressed as:

$$\Delta\mathbf{E}_{ik}^{\mathrm{sc}} \simeq \frac{j\omega}{J_i \Delta S_i} \int_S \Delta\varepsilon(\mathbf{r}', t_0, t_1)\, \mathbf{E}_i^{\mathrm{inc}}(\mathbf{r}')\, \mathbf{E}_k^{\mathrm{inc}}(\mathbf{r}')\, dS'. \tag{4}$$

Both incident fields, $\mathbf{E}_i^{\mathrm{inc}}$ and $\mathbf{E}_k^{\mathrm{inc}}$, can be obtained either through numerical simulations or measurements [27] from a representative reference background, i.e., the patient-specific head tissues. However, from a practical point of view, no direct measurements of the field distribution in S are available; therefore, the incident fields in (4) are typically evaluated using forward electromagnetic simulations of a reference known model, usually corresponding to the healthy head tissues. Thus, the accuracy of image reconstruction depends, among other factors, on how well the computational model mimics the conditions under which the differential data $\Delta E_{ik}^{\mathrm{sc}}$ are acquired. Any mismatch between the simulated and the real head anatomy, including the tissue permittivity distribution, or antenna coupling, introduces a modeling error that propagates directly into the inverse problem, and consequently into $\Delta\varepsilon(\mathbf{r}, t_0, t_1)$.

To compute a numerical solution of (4), the imaging domain S is discretized into N_c triangular cells, each of area Δs. Thus (4) becomes:

$$\Delta\mathbf{E}_{ik}^{\mathrm{sc}} \simeq \frac{j\omega}{J_i \Delta S_i} \sum_{j=1}^{N_c} \Delta\varepsilon(\mathbf{r}_j, t_0, t_1)\, \mathbf{E}_i^{\mathrm{inc}}(\mathbf{r}_j)\, \mathbf{E}_k^{\mathrm{inc}}(\mathbf{r}_j)\, \Delta s_j, \tag{5}$$

where $\mathbf{r}_j$ is the centroid of the j-th cell. For a multi-static system configuration with N_{a} antennas or probes, where $i, k \in \{1, ..., N_{\mathrm{a}}\}$, (5) can be written in a compact matrix form as:

$$[\Delta\mathbf{E}^{\mathrm{sc}}] = [\mathbf{K}]\, [\Delta\varepsilon], \tag{6}$$

where $[\Delta\mathbf{E}^{\mathrm{sc}}]$ is a $N_{\mathrm{a}}^2 \times 1$ vector collecting the differential scattered field for all receiver-transmitter pairs (i, k), $[\Delta\varepsilon]$ is a $N_c \times 1$ vector representing the unknown permittivity contrast associated with the temporal evolution of the stroke in each j-th cell, and $[\mathbf{K}]$ is $N_{\mathrm{a}}^2 \times N_c$ linear operator whose each single element $\kappa_{(i,k),j}$ is defined as:

$$\kappa_{(i,k),j} = \frac{j\omega}{J_i \Delta S_i}\, \mathbf{E}_i^{\mathrm{inc}}(\mathbf{r}_j)\, \mathbf{E}_k^{\mathrm{inc}}(\mathbf{r}_j). \tag{7}$$

B. Truncated Singular Value Decomposition Imaging

The linear system in (6) is ill-conditioned and ill-posed, even assuming full anatomical prior acknowledgment, and the direct inversion of $\mathbf{K}$ leads to unstable solutions. To regularize and stabilize the solution, the TSVD approach [6] is used:

$$[\Delta\varepsilon] \simeq \sum_{n=1}^{T} \frac{1}{\sigma_n} \left([u_n]^* [\Delta\mathbf{E}^{\mathrm{sc}}]\right) [v_n], \tag{8}$$

where $[\cdot]^*$ indicates the conjugate transpose, σ_n, $[u_n]$, and $[v_n]$ are the n-th singular value, left, and right singular vectors, respectively, obtained via the singular value decomposition (SVD) of the discretized operator $[\mathbf{K}]$. Specifically, the TSVD is applied to the linearized operator obtained under the distorted Born approximation since, during monitoring, the reference model used for linearization is a distorted version of the actual situation. The truncation index T acts as a regularization parameter and is determined using a threshold defined in terms of the cumulative energy of the first n singular values [28], [29]. Since the singular values decay quickly, most of the energy corresponds to the first n singular values. Therefore, we adopt a conservative threshold corresponding to 99.99% of the cumulative energy, which balances solution stability and image quality.

C. Imaging metrics

In MMWI, the quality of the retrieved maps is important for accurate diagnosis and treatment planning. Qualitative microwave imaging (MWI) algorithms aim to identify the presence, spatial location, extent, and morphology of anomalies in the background tissue, providing clinically relevant information that, depending on the application, may be sufficient. Additionally, quantitative MWI algorithms aim

This work is licensed under a Creative Commons Attribution-NonCommercial-NoDerivatives 4.0 License.
For more information, see https://creativecommons.org/licenses/by-nc-nd/4.0/

This article has been accepted for publication in IEEE Open Journal of Antennas and Propagation. This is the author's version which has not been fully edited and content may change prior to final publication. Citation information: DOI 10.1109/OJAP.2026.3724057

to reconstruct complex-valued dielectric contrast maps, providing complementary information on tissue properties that may indicate relevant clinical information, such as stroke typology. Regardless of the algorithm, image quality is essential in medical scenarios. In line with criteria adopted in neuroimaging [30], [31], a MWI reconstruction can be considered acceptable for medical diagnosis if its spatial resolution can accurately delineate the location, extent, and morphology of the expected dielectric variations, such as the caused by a ICH or AIS progression, if it exhibits sufficient contrast relative to the background, i.e., healthy tissues. For quantitative reconstructions, the real and imaginary parts of the contrast map should also be consistent with the expected values. When a reference image is available, such as in controlled experiments to validate MWI systems and algorithms, it is also possible to assess the global structural similarity between the reconstructed and reference maps, as well as the linear correlation between their respective distributions. Accordingly, various imaging metrics are used to quantify the quality of the retrieved contrast maps.

For qualitative evaluation of MWI reconstructions, as in [15], a binarized form of the MWI reconstructions is compared with a known binary ground truth. However, selecting the binarization threshold for the qualitative reconstructions is nontrivial because the images are subject to the inherent smoothing associated with the necessary regularization [32]. To address this, we use the spatial resolution criteria of the MWI system itself as the binarization metric, which is approximately equal to the half width of the image point-spead function (IPSF) main lobe, proportional at $-4\,\mathrm{dB}$ relative to its peak value [33]. Values above this threshold are considered regions where a permittivity contrast arises due to actual scatterers. Accordingly, any value in the qualitative MWI reconstructions above $-4\,\mathrm{dB}$ is set to 0 and 1 otherwise.

To compute the imaging performance metrics, let $\mathcal{A} = \Delta\varepsilon_r$, the reconstructed complex permittivity contrast map, where $\varepsilon_r = \varepsilon/\varepsilon_0$ is the complex relative permittivity, $\mathbf{A}$ its normalized version, and $\widehat{\mathbf{A}} \in \{0,1\}$ the binarized version one. Instead, $\mathcal{B}$ is the expected relative permittivity contrast map, i.e., the ground truth, $\mathbf{B}$ its normalized version, and $\widehat{\mathbf{B}} \in \{0,1\}$ the binarized version. The binarized reconstructed and the ground truth mask are vectors where $\widehat{\mathbf{A}} = [\widehat{a}_0, \widehat{a}_1, ..., \widehat{a}_j]$ and $\widehat{\mathbf{B}} = \left[\widehat{b}_0, \widehat{b}_1, ..., \widehat{b}_j\right]$, with $\widehat{a}_j$ and $\widehat{b}_j$ the j-th cell position values. The lesion area has values of 1, and the non-lesion one has values of 0. The metrics used to evaluate the MWI reconstructions are described in the following:

1) Dice Similarity Coefficient (DSC)

The Dice Similarity Coefficient (DSC) [15], [34], [35] evaluates the fraction of overlap between the reconstructed and ground-truth stroke progression regions, i.e., between $\widehat{\mathbf{A}}$ and $\widehat{\mathbf{B}}$, normalized by the total number of cells with 1 values in both sets:

$$\mathrm{DSC} = \frac{2\sum_{j=1}^{N_c} \widehat{a}_j\, \widehat{b}_j}{\sum_{j=1}^{N_c} \left(\widehat{a}_j + \widehat{b}_j\right)}. \tag{9}$$

The DSC ranges from 0, indicating no overlap, to 1, indicating a perfect match between the binarized reconstruction and ground truth.

2) Boundary-Based Metric (BBM)

The boundary-based metric (BBM), presented in [15] is a normalized Hausdorff distance (HD) on its 95% percentile (HD95) [36], [37], which is widely used in medical imaging to delineate the boundary errors of anatomical structures; variations of HD have been used in other studies [18], [35]. The metric is computed as follows: HD computes the maximum of all shortest distances from all points in $\widehat{\mathbf{A}}$ to the points in $\widehat{\mathbf{B}}$. Then, HD95 calculates the 95th percentile of these distances to avoid outliers. Finally, HD95 is normalized with respect to the maximum Euclidean distance, $D_{\max}$, between $\widehat{\mathbf{A}}$ and $\widehat{\mathbf{B}}$.

To compute the BBM, let $\mathcal{C}_{\widehat{A}} = \{\mathbf{r}_j : \widehat{a}_j = 1\}$ and $\mathcal{C}_{\widehat{B}} = \{\mathbf{r}_j : \widehat{b}_j = 1\}$ denote the sets of cells coordinates in $\widehat{\mathbf{A}}$ and $\widehat{\mathbf{B}}$, respectively, where $\mathbf{r}_j$ is the spatial position of the j-th cell in the DoI. The 95th-percentile Hausdorff distances are calculated as:

$$h_{\widehat{A}} = \mathrm{P}_{95}\left\{ \min_{\mathbf{r} \in \mathcal{C}_{\widehat{B}}} \|\mathbf{r}_j - \mathbf{r}\|_2 \;:\; \mathbf{r}_j \in \mathcal{C}_{\widehat{A}} \right\}, \tag{10}$$

$$h_{\widehat{B}} = \mathrm{P}_{95}\left\{ \min_{\mathbf{r} \in \mathcal{C}_{\widehat{A}}} \|\mathbf{r}_j - \mathbf{r}\|_2 \;:\; \mathbf{r}_j \in \mathcal{C}_{\widehat{B}} \right\}, \tag{11}$$

where $\mathrm{P}_{95}\{\cdot\}$ denotes the 95th percentile over the set of minimum distances, and $\|\cdot\|_2$ is the ℓ_2 norm, i.e., the Euclidean distance. To obtain a normalized metric, the maximum spatial extent of the combined regions $\mathcal{C}_{\widehat{A}}$ and $\mathcal{C}_{\widehat{B}}$ is used as a normalization factor and defined as:

$$D_{\max} = \max_{\mathbf{r}_i, \mathbf{r}_j \in \mathcal{C}_{\widehat{A}} \cup \mathcal{C}_{\widehat{B}}} \|\mathbf{r}_i - \mathbf{r}_j\|, \tag{12}$$

which represents the largest possible distance within the union of the reconstructed and reference regions. The BBM is then defined as:

$$\mathrm{BBM} = 1 - \frac{\max(h_{\widehat{A}},\, h_{\widehat{B}})}{D_{\max}}, \tag{13}$$

where a value closer to 1 corresponds to perfect morphological consistency, meaning that the reconstructed and reference stroke regions closely match in both shape and boundary, whereas a value of 0 indicates no morphological consistency.

3) Structural Similarity Index (SSIM)

The structural similarity index (SSIM) [16] measures the global perceived image similarity between the binarized reconstruction $\widehat{\mathbf{A}}$ and ground truth $\widehat{\mathbf{B}}$. This metric intends to approximate how humans perceive the difference between two images, with particular sensitivity to the shape, spatial

This work is licensed under a Creative Commons Attribution-NonCommercial-NoDerivatives 4.0 License.
For more information, see https://creativecommons.org/licenses/by-nc-nd/4.0/

This article has been accepted for publication in IEEE Open Journal of Antennas and Propagation. This is the author's version which has not been fully edited and content may change prior to final publication. Citation information: DOI 10.1109/OJAP.2026.3724057

distribution, and continuity of the stroke region. The SSIM is defined as:

$$\mathrm{SSIM} = \frac{(2\alpha_{\widehat{A}}\alpha_{\widehat{B}} + c_1)(2\beta_{\widehat{A}\widehat{B}} + c_2)}{(\alpha_{\widehat{A}}^2 + \alpha_{\widehat{B}}^2 + c_1)(\beta_{\widehat{A}}^2 + \beta_{\widehat{B}}^2 + c_2)}, \tag{14}$$

where $\alpha_{\widehat{A}}$ and $\alpha_{\widehat{B}}$ are the mean values of $\widehat{\mathbf{A}}$ and $\widehat{\mathbf{B}}$, respectively, $\beta_{\widehat{A}}^2$ and $\beta_{\widehat{B}}^2$ are their variances, $\beta_{\widehat{A}\widehat{B}}$ is their cross-covariance, $c_1 = (0.01\,L)^2$ and $c_2 = (0.03\,L)^2$ are stabilization terms that prevent numerical instability in regions with near-zero mean or variance, and $L = 1$ denotates the dynamic range of the binary inputs $\widehat{A}$ and $\widehat{B}$. The SSIM has been used in some studies to evaluate MWI repeatability [18], [38], and imaging performance assessment [39], [40]. The SSIM is bounded from 0, no similarity, to 1, perfect similarity between the binarized MWI reconstruction and the expected one.

4) Contrast-to-Noise-Ratio (CNR)

The contrast-to-noise ratio (CNR) [41] is an object-independent metric widely used to quantify the detectability of a target against a background. It provides a measure of how distinguishable a dielectric contrast is with respect to the surrounding medium. In the brain stroke monitoring context, CNR evaluates the difference between the mean values within the expected contrast area, i.e., to injury evolving, and that of the background, divided by the standard deviation of the background:

$$\mathrm{CNR_A} = \frac{|\alpha_{A_s} - \alpha_{A_b}|}{\beta_A}, \tag{15}$$

where α_{A_s} and α_{A_b} are the mean values of $\mathbf{A}$ in the expected stroke region and the background region, respectively, and β_{A_b} is the standard deviation of $\mathbf{A}$ in the background region. The CNR range is $[0, +\infty)$, with higher values indicating greater contrast of the lesion region. To enable meaningful comparisons across other image performance metrics and inversion kernels, the CNR is normalized to the CNR obtained from the ideal image point spread function (IPSF), computed in a homogeneous background with no model mismatch, tissue heterogeneity, or structural approximation. Thus, in this reference case, $\mathrm{CNR_{IPSF}}$ can be considered as the upper bound of the achievable CNR for the given system configuration. The normalized $\mathrm{CNR_N}$ is therefore defined as:

$$\mathrm{CNR_N} = \frac{\mathrm{CNR_A}}{\mathrm{CNR_{IPSF}}}. \tag{16}$$

Consequently, $\mathrm{CNR_N} = 1$ means that the MWI reconstruction reproduces the lesion-to-background contrast of an ideal IPSF response, whereas $\mathrm{CNR_N} < 1$ indicates a contrast loss, possibly due to model errors, tissue heterogeneity, or kernel inaccuracies.

5) Peak-Signal-to-Noise-Ratio (PSNR)

The peak-signal-to-noise ratio (PSNR) [42] is a widely used metric in MMWI [43], [44]. In brain stroke imaging, it quantifies the ratio between the maximum image intensity and the mean squared error (MSE) relative to the reference image, reflecting how accurately the reconstructed map preserves the lesion-related intensity distribution. PSNR is defined as:

$$\mathrm{PSNR} = \frac{\max(\mathbf{A})^2}{\mathrm{MSE}}, \tag{17}$$

where $\mathrm{MSE} = \frac{1}{N_c}\sum_{i=1}^{N_c}(A_i - \widehat{B}_i)^2$ is the mean squared error between the reconstructed image $\mathbf{A}$ and the reference image $\widehat{\mathbf{B}}$. The PSNR range is $[0, +\infty)$, where larger values correspond to higher contrast. To enable comparisons with other image performance metrics, the PSNR is normalized to the PSNR obtained from the ideal image point spread function (IPSF), calculated from a simulation campaign using a homogeneous head model whose dielectric properties correspond to a weighted average of the head tissues. The normalized PSNR is therefore defined as:

$$\mathrm{PSNR_N} = \frac{\mathrm{PSNR}_A}{\mathrm{PSNR_{IPSF}}}, \tag{18}$$

where $\mathrm{PSNR_N}$ values closer to 1 mean that the reconstructed stroke-related intensity distribution is comparable to that of an ideal IPSF response, whereas $\mathrm{PSNR_N} < 1$ indicates a high deviation from the ideal IPSF response.

6) Pearson Correlation Coefficient (PCC)

The Pearson correlation coefficient (PCC) is a statistical measure of linear similarity between two images or signals. In MMWI [45], it quantifies the degree of linear correspondence between the reconstructed and reference intensity distributions. It is defined as:

$$\mathrm{PCC} = \frac{\sum_{j=1}^{N_c}(a_j - \alpha_A)(b_j - \alpha_B)}{\sqrt{\sum_{j=1}^{N_c}(a_j - \alpha_A)^2}\sqrt{\sum_{j=1}^{N_c}(b_j - \alpha_B)^2}}, \tag{19}$$

where a_j and b_j are the j-th elements of $\mathbf{A}$ and $\mathbf{B}$, respectively, and α_A and α_B are their mean values over all N_c cells.

A PCC value of 1 indicates perfect linear correlation, 0 no correlation, and -1 perfect anti-correlation. Thus, PCC values of 1 indicate perfect linear correlation between the reconstructed and expected distributions, i.e, that the nature of the stroke progression is correctly identified, and values closer to 0 indicate no linear correlation. Across all evaluated monitoring scenarios considered in this work, only positive PCC values are observed.

7) Normalized Root-Mean-Square-Error (NRMSE)

The normalized root mean square error (NRMSE) has been used in various MMWI applications [18], [46], [47], and measures the average per-cell magnitude of discrepancy between the reconstructed map $\boldsymbol{\mathcal{A}}^{(\cdot)}$ and the ground truth $\boldsymbol{\mathcal{B}}^{(\cdot)}$. It is defined as:

$$\mathrm{NRMSE}_{(\cdot)} = \frac{\sqrt{\frac{1}{N_C}\sum_{j=1}^{N_C}\left(\mathcal{A}_j^{(\cdot)} - \mathcal{B}_j^{(\cdot)}\right)^2}}{\Delta_{(\cdot)}}, \tag{20}$$

This work is licensed under a Creative Commons Attribution-NonCommercial-NoDerivatives 4.0 License.
For more information, see https://creativecommons.org/licenses/by-nc-nd/4.0/

This article has been accepted for publication in IEEE Open Journal of Antennas and Propagation. This is the author's version which has not been fully edited and content may change prior to final publication. Citation information: DOI 10.1109/OJAP.2026.3724057

where the superscript $(\cdot)$ denotes either the real or imaginary part, dubbed R and I, respectively. The normalization term is defined as $\Delta_{(\cdot)} = \min(\delta_{\mathcal{A}^{(\cdot)}}, \delta_{\mathcal{B}^{(\cdot)}})$, where:

$$\delta_{\zeta^{(\cdot)}} = \max(\boldsymbol{\zeta}^{(\cdot)}) - \min(\boldsymbol{\zeta}^{(\cdot)}) : \zeta \in \{\mathcal{A}, \mathcal{B}\}, \tag{21}$$

denotes the dynamic ranges of the corresponding components.

The NRMSE ranges from 0, representing no difference, to 1, representing the maximum difference in the reconstructed permittivity contrast map. To avoid ambiguous analysis relative to the other metrics, we introduce $\mathrm{NRMSE_N} = 1 - \mathrm{NRMSE}$, with values between 0 and 1 indicating the maximum and minimum error, respectively. $\mathrm{NRMSE_N}$ is computed separately on the real and imaginary parts of the complex permittivity contrast.

Each metric used in this work evaluates a particular characteristic of the reconstructed images. Specifically, they measure how accurately the spatiotemporal variations in the dielectric properties of brain tissues caused by the evolution of an ICH or AIS match the expected ones, in terms of localization, size, shape, overlap, structural similarity, statistical dependence, and contrast. Overall, this study considers eight metrics: six to evaluate the quality of the qualitative reconstructions, and two to evaluate the quantitative accuracy of the retrieved contrast maps.

D. Spearman Weighted Metric (SWM)

All the metrics described in the previous section provide valuable feature-specific information about imaging performance; however, as individual metrics, they lack the cohesiveness and fidelity that a comprehensive, multi-metric approach can offer. Nonetheless, a naive approach, such as an even-averaged one, may yield biased outcomes because, if similar features are measured by more than one metric, they weigh more in a simple overall average. To address this issue, here we propose a correlation-aware weighted Spearman correlation coefficient, hereafter referred to as the Spearman weighted metric (SWM). The Spearman correlation captures monotonic relationships between the metrics without assuming linearity, which is appropriate given the non-linear nature of the studied scenario. SWM computes the Spearman correlation matrix among the imaging metrics under consideration. Specifically, this study uses the eight aforementioned metrics. Then, the weights are computed from the correlation matrix, penalizing highly correlated pairs and rewarding less correlated pairs. Finally, the weights are merged into a single balanced score.

The core of the SWM lies in the problem-specific correlation matrix and in its construction. As a generalist approach, we propose using a significant and representative inverse-scattering scenario for the problem at hand.

The Spearman correlation matrix ranges from -1 to 1, where 0 indicates no correlation, and 1 and -1 indicate perfect positive and negative correlations, respectively. Only positive values are observed in this study. The proposed SWM is computed as follows: let $\rho_{p,n}$ represent a single entry of the Spearman correlation coefficient between the p-th and n-th metrics. We define:

$$c_p = \sum_{\substack{n=1 \\ n \neq p}}^{M} \rho_{p,n}, \tag{22}$$

representing the sum of the correlations between the p-th metric and all the other metrics, where M is the total number of imaging metrics. The weight associated with the p-th metric is then defined as:

$$w_p = \frac{1}{c_p}, \tag{23}$$

and the final score, SWM, is computed as the weighted average of the metrics:

$$\mathrm{SWM} = \frac{\sum_{p=1}^{M} w_p \, m_p}{\sum_{p=1}^{M} w_p}, \tag{24}$$

where m_p denotes the p-th metric value. Thus, metrics that are less correlated with the others receive larger weights and therefore contribute more to the final score, while highly correlated metrics are down-weighted. The resulting weights for each metric are then used to calculate and report the SWM values across all studied cases.

III. FRAMEWORK ASSESSMENT

A. Clinical Scenario

To generalize anatomical complexity and obtain a non-patient-dependent conclusion, we consider an anatomical baseline comprising 20 human adult subjects. These consist, each, of a realistic segmented head model with eleven segmented tissue classes [48], respectively named, cerebrospinal fluid (CSF), gray matter, white matter, fat, muscle, muscle/skin, skull, blood vessels, peripheral fat, dura mater, and bone marrow, from which a single sagittal slice is extracted. These models are defined as DoI and have an isotropic spatial resolution of $0.5\,\mathrm{mm}$ per pixel. Figure 1 shows an example of a sagittal slice with the corresponding dielectric properties (all the other sliced models used are available in the supplementary materials). The tissues' dielectric properties are assigned according to the values reported in [49], and depicted in Fig. 2, where the shaded regions represent a $\pm 5\%$ uncertainty band around the nominal values, accounting for the inter-subject biological variability. However, it is worth noting that the uncertainty-aware dielectric prior remains, as the actual patient-specific information is unavailable.

To emulate the stroke spatiotemporal evolution, the dielectric properties of the pixels indicating the progressing lesion region are modified to match those of blood for ICH, and are set to 10% below the reference tissue properties for AIS.

A similar approach has been adopted in previous works [50], [51]. Table 1 reports the real part, $\Delta\varepsilon_r'$, and imaginary part, $\Delta\varepsilon_r''$, of the relative complex permittivity contrast $\Delta\varepsilon_r = \varepsilon_r^{(\mathrm{lesion})} - \varepsilon_r^{(\mathrm{tissue})}$ between the stroke lesion and the surrounding gray and white matter at 1 GHz.

This work is licensed under a Creative Commons Attribution-NonCommercial-NoDerivatives 4.0 License.
For more information, see https://creativecommons.org/licenses/by-nc-nd/4.0/

This article has been accepted for publication in IEEE Open Journal of Antennas and Propagation. This is the author's version which has not been fully edited and content may change prior to final publication. Citation information: DOI 10.1109/OJAP.2026.3724057

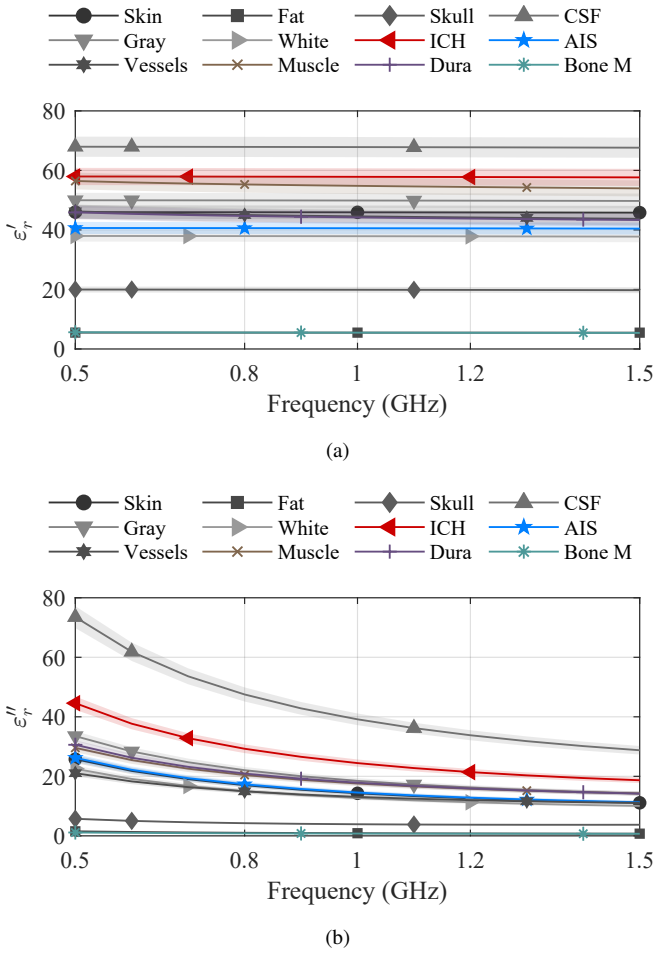

FIGURE 2. **Frequency-dependent dielectric properties of head tissues: (a) real part and (b) imaginary part of ε_r. Bone marrow is dubbed Bone M.**

TABLE 1. **Dielectric contrast at 1 GHz between stroke and brain tissues.**

	ICH		AIS	
	Gray matter	**White matter**	**Gray matter**	**White matter**
$\Delta\varepsilon_r'$	-7.96	-19.95	5.25	3.86
$\Delta\varepsilon_r''$	5.96	11.74	-1.77	-1.12

Three lesion morphologies are considered. First, a capsule-like one that accounts for unidirectional axial progression. Second, a circular model in which lesions expand radially from a focal origin. The third is a realistic anthropomorphic shape, derived from a clinical MRI previously evaluated in [52], [53], which captures the axial and radial growth of stroke lesions and accounts for the irregular evolution of strokes. These are named CAP, SPH, and ANM, respectively, from here on. All lesions are placed in the left lateral hemisphere at three distinct locations, as shown in Fig. 3. These locations correspond to a clinically relevant brain region, the middle cerebral artery (MCA) extension, which is commonly involved in stroke pathology [54], [55]. The spatial coordinates of the three positions, denoted as C1, C2, and C3, are detailed in Table 2.

TABLE 2. **Coordinates of the centers for the SPH/ANM and CAP configurations. The x coordinate is fixed at -32 mm for all cases.**

	SPH / ANM			CAP		
	C1	**C2**	**C3**	**C1′**	**C2′**	**C3′**
y	-46	4	54	-29	16	61

B. Problem Setup

For simulation, we employ an in-house two-dimensional (2-D) finite element method (FEM) EM solver. The simulations are conducted with $N_a = 48$ line-source elements serving as both transmitting and receiving antennas, uniformly distributed around the DoI as shown in Fig. 1. The simulated data are then sub-sampled in post-processing to synthetically reduce the antenna array size to $N_a \in \{24, 18, 12\}$, later used to analyze the effect of N_a, while maintaining the uniform angular distribution of the elements around the DoI. For the differential scattered field data $\Delta\mathbf{E}^{\text{sc}}$ in (6), the reference head models use the original isotropic spatial resolution of $0.5\,\text{mm}$ per pixel, as well as eleven tissues, and so represents the best (optimistic) scenario in which full patient-specific anatomical information is available. Additionally, the dielectric properties of all tissues are considered to have an intra-tissue variability within $\pm 5\%$. Conversely, the imaging kernel $\mathbf{K}$ is built from forward simulations performed at coarser spatial resolutions of 1, 2, 3, and $4\,\text{mm}$ per pixel. Note that assuming a different mesh and inter-tissue dielectric variability avoids the *inverse crime* and makes the whole approach more robust and realistic. Then, the mesh discretization of the DoI uses a structured triangular mesh, in which each pixel of the reference head models is subdivided into two triangles, so that the input pixel size of the head models directly determines the mesh resolution and limits meshing interpolation errors. Moreover, to allow the freedom to select any location for the line-source elements, we use an unstructured mesh outside the DoI.

An important requirement for a stroke-monitoring MMWI system is to maximize the amount of incident power that penetrates the head, so that sufficiently strong scattered signals from the stroke can be collected outside the head, enabling imaging. This is commonly achieved by using a matching medium to maximize wave penetration. An additional requirement is to achieve the highest possible spatial resolution, given the system's operating frequency, to identify sufficiently small variations. Thus, the selection of both the operating frequency and the matching medium is critical, and a non-trivial one, though. In this respect, in [56], [57], analytical studies have been performed by using simplified multi-layer models, finding the band around 1 GHz and a matching medium permittivity of 20 a good trade-off candidate. However, to extend this conclusion to a more realistic and complex scenario, in this work, we consider a 2D scenario shown in Fig. 1, selecting the line-source element at 12 o'clock (the red one in Fig. 1), which is placed approximately at $20.5\,\text{mm}$ from the head contour, and

This work is licensed under a Creative Commons Attribution-NonCommercial-NoDerivatives 4.0 License.
For more information, see https://creativecommons.org/licenses/by-nc-nd/4.0/

This article has been accepted for publication in IEEE Open Journal of Antennas and Propagation. This is the author's version which has not been fully edited and content may change prior to final publication. Citation information: DOI 10.1109/OJAP.2026.3724057

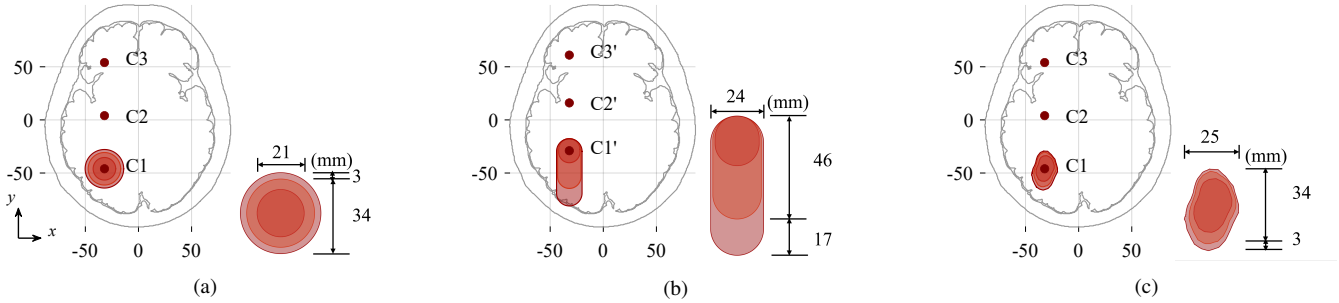

FIGURE 3. **Different stroke morphologies and positions. a) SPH, b) CAP, and c) ANM. The coordinates of the center positions are reported in Table 2. For the spherical and anthropomorphic cases, the positions are identical, whereas for the CAP case, these are shifted posteriorly to ensure that all configurations lie within the brain. The dimensions are in mm.**

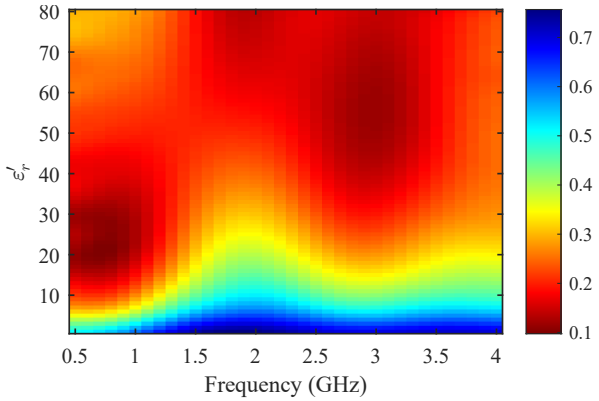

FIGURE 4. **Normalized-Reflection coefficient Γ versus matching medium ε_r' and frequency (GHz).**

perform a parametric study in a lossless matching medium varying the real part of the relative complex permittivity of the matching medium, ε_r', from 1 to 80 at different operating frequencies from 0.5 to 4 GHz.

Three different scenarios are simulated: an eleven-tissue head model surrounded by matching medium, a scenario in which the head region is a perfect electric conductor (PEC), and a homogeneous background filled with matching medium. In each parametric simulation, the field is collected in the coordinates of the transmitting probe, and a normalized reflection coefficient is defined as:

$$\Gamma = \frac{\left|E^{\text{tot}}_{\text{MT}} - E^{\text{inc}}\right|}{\left|E^{\text{tot}}_{\text{PEC}} - E^{\text{inc}}\right|}, \tag{25}$$

where $E^{\text{tot}}_{\text{MT}}$ and $E^{\text{tot}}_{\text{PEC}}$ are the total electric field at the probe location for the multi-tissue head model and PEC head model, respectively, and E^{inc} is the incident field in the homogeneous background. The numerator denotes the scattered field produced by the head tissues, while the denominator normalizes it with respect to the scattered field of the PEC scenario; the latter provides a reference for the maximum reflected field in the direction to the probe position. Accordingly, Γ indicates how much energy is reflected by the head tissues with respect to the field reflected by a PEC. Since $\Gamma \leq 1$, it follows from (25) that $|E^{\text{sc}}_{\text{MT}}| \leq |E^{\text{sc}}_{\text{PEC}}|$. The results are shown in Fig. 4. Higher reflections are observed in the absence of a matching medium, i.e., when $\varepsilon_r' = 1$. For the relative permittivity of the matching medium below $\varepsilon_r' \approx 10$, higher reflections are present across almost the entire frequency range. A frequency band with high reflections is observed roughly between 1.5 and 2.5 GHz for $\varepsilon_r' < 40$, suggesting impedance mismatch. At frequencies above 3.5 GHz with $\varepsilon_r' > 40$, the reflections decrease; however, in this frequency band, the field penetration depth into the head tissues is minimal due to the high dielectric losses in biological tissues, making such conditions unfavorable for detecting anomalies in deep brain tissues.

These results are consistent with those obtained from a simplified cross-section of the head tissues studied in [56], [57], confirming the validity of the analysis. It is worth noting that at frequencies below 1 GHz, the reflections are reduced for some ε_r' values, but the spatial resolution is correspondingly reduced. Based on these findings, the operating conditions used in the remainder of this study are a frequency of 1 GHz and a matching medium with $\varepsilon_r' = 20$, which offers a good trade-off between spatial resolution and impedance matching to head tissues.

C. Inversion Kernels

To evaluate the impact of prior anatomical information, structural and dielectric encoding, on imaging retrieval, we establish five inversion kernels $\mathbf{K}$, guided by practical limitations in real clinical scenarios, in which neuroimaging modalities, such as MRI and CT, may not be routinely available, and have intrinsic well-known and limiting difficulties of accurately segmenting head tissues [58]. MRI provides strong soft-tissue contrast [58], [59] and enables good discrimination of the most of intracranial tissues [58], [60]. CT provides good contrast for osseous structures [61] such as the skull, but limited discrimination of the surrounding soft tissues due to their similar Hounsfield unit ranges [62] making the external tissues, i.e., skin, fat and skull, difficult to segment individually. Then, to build the kernels, the eleven-tissue head models are systematically reduced, retaining only the tissues that can be segmented most

This work is licensed under a Creative Commons Attribution-NonCommercial-NoDerivatives 4.0 License.
For more information, see https://creativecommons.org/licenses/by-nc-nd/4.0/

This article has been accepted for publication in IEEE Open Journal of Antennas and Propagation. This is the author's version which has not been fully edited and content may change prior to final publication. Citation information: DOI 10.1109/OJAP.2026.3724057

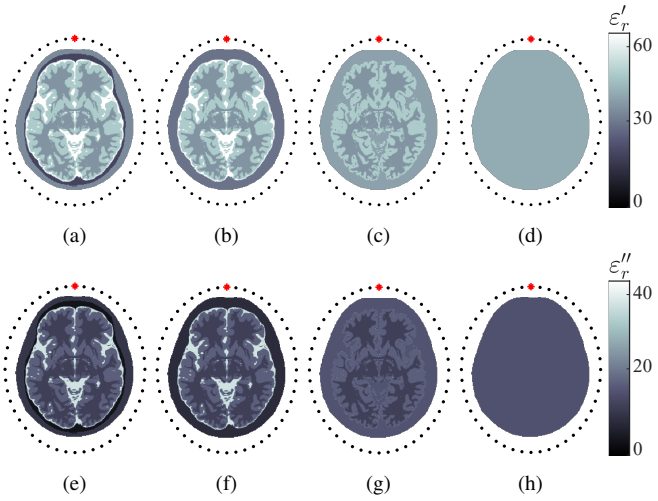

FIGURE 5. **Inversion kernels. The real part ε'_r is shown in the top row, and the imaginary part ε''_r in the bottom row. Columns correspond to the kernel K_A, K_B, K_C, and K_H. For visualization, the head maps are displayed at 35% smaller visual scale than in Fig. 1. K_{MT} is reported in Fig. 6.**

reliably. These models are shown in Fig. 5 and summarized in Table 3, where the vertical bar (|) marks tissue boundaries and the plus sign (+) indicates tissues merged into a single equivalent tissue whose dielectric properties are the area-weighted average of the constituents.

TABLE 3. **Inversion kernel operators for the assessment.**

Kernel	Reference head model
K_{MT}	Skin† | Fat | Bone‡ | CSF | Gray matter | White matter*
K_{A}	Skin† + Fat | Bone‡ | CSF | Gray matter | White matter*
K_{B}	Skin† + Fat + Bone‡ | CSF | Gray matter | White matter*
K_{C}	Skin† + Fat + Bone‡ + CSF | Gray matter | White matter*
K_{H}	Skin† + Fat + Bone‡ + CSF + Gray matter + White matter*

†Skin: skin + muscle; ‡Bone: skull + bone M + dura; *White matter: white + vessels
See Fig. 2 for the tissue names.

The kernel K_{MT}, which incorporates the most prior information, considers six "tissues", and may account for cases where MRI and CT simplified priors are available. The kernel K_{A} accounts for a common limitation in MRI-based segmentation where the external tissue layers, i.e., skin and subcutaneous fat, are anatomically thin and spatially adjacent, making their mutual delineation challenging [58], [63], [64]. Therefore, the skin and fat are merged into a single equivalent tissue, whose dielectric properties are given as the area-weighted average of the two tissues. A model in which the skin, fat, and skull are merged into a single tissue can also be considered realistic, and therefore, the kernel K_{B} is also studied here. Moreover, the kernel K_{C} accounts for a limitation arising from the nature of the CSF, which is anatomically thin, typically between 1 and 3 mm, comparable to the voxel size in low-resolution CT, MRI, or PET scans [65], [66], making its segmentation difficult. Accordingly, the CSF is merged with the external

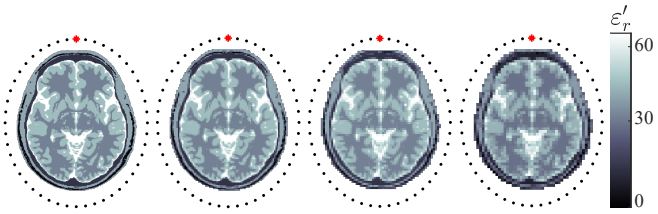

FIGURE 6. **Different resolutions of the K_{MT} for ε'_r: (a) 1 mm, (b) 2 mm, (c) 3 mm, and (d) 4 mm. For visualization, the head maps are displayed at 35% smaller visual scale than in Fig. 1.**

tissues, skin, fat, and skull. The kernel K_{H} represents the less favorable case when no prior information, apart from the head shape, is available. All tissues are merged into a single homogeneous medium, whose dielectric properties are the area-weighted average of all constituent tissues. Although simplified, it offers the significant advantage of being available in most clinical settings.

For each of the kernels described above, we evaluate four isotropic pixel sizes: 1, 2, 3, and 4 mm, which directly define the mesh resolution of the DoI in the forward simulations to build the kernels. Resolutions of 1 and 2 mm are typically considered the standard in CT and MRI acquisitions. Resolutions of 3 and 4 mm are common in conventional clinical MRI and CT when acquisition time is reduced, in low-field MRI systems, and in PET scans [65]–[67]. Regardless of the quality of the available prior information, the following question arises: is a high-resolution anatomical prior strictly necessary for accurate microwave imaging in brain stroke monitoring, or can a coarser structural model of head tissues, with an inherently reduced computational cost, still provide sufficient information for accurate monitoring of an ICH or AIS lesion? The results addressing this question are presented in Sect. IV.

D. Spearman correlation matrix

To quantitatively evaluate the performance of the kernels described above, the SWM, described in Sect. II-D, is used. For this purpose, the Spearman correlation matrix across all imaging performance metrics is required to compute SWM. Therefore, we consider as a representative inverse-scattering scenario a homogeneous head whose dielectric properties are the weighted average of the tissues, and 51 circular ICH and AIS lesions distributed across it, each with a diameter $\lambda_b/4 \approx 1.2$ cm, where λ_b is the wavelength of the background medium. This diameter corresponds to the minimum spatial resolution of first-order Born and Rytov approximations for tomographic-based imaging [68], [69]. Hence, to consider the best-performing case, the imaging is performed by projecting the ICH and AIS contrasts into the truncated $\mathbf{K}$ operator.

Figure 7 reports the Spearman correlation coefficients among the adopted metrics for both stroke types. The lower triangular part of the matrix, shown in red, contains the

This work is licensed under a Creative Commons Attribution-NonCommercial-NoDerivatives 4.0 License.
For more information, see https://creativecommons.org/licenses/by-nc-nd/4.0/

This article has been accepted for publication in IEEE Open Journal of Antennas and Propagation. This is the author's version which has not been fully edited and content may change prior to final publication. Citation information: DOI 10.1109/OJAP.2026.3724057

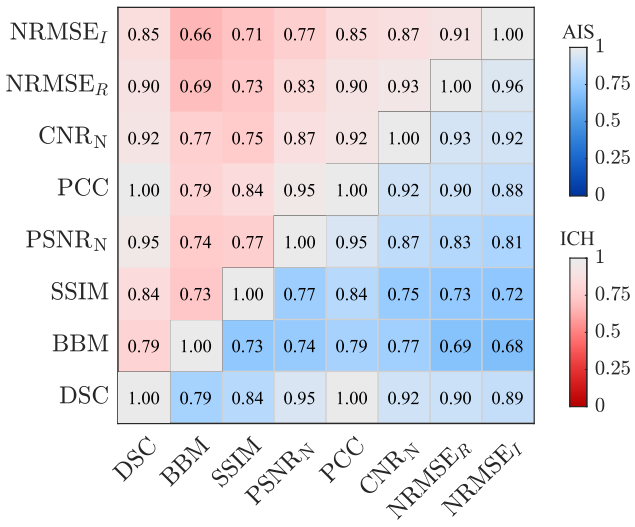

FIGURE 7. Spearman correlation coefficients among the eight imaging metrics. The lower triangular part, shown in red, reports the ICH coefficients, whereas the upper triangular part, shown in blue, reports the AIS coefficients.

coefficients obtained for ICH, whereas the upper triangular part, shown in blue, contains those obtained for AIS. Each stroke-specific correlation matrix is individually symmetric. However, the combined matrix is not expected to be completely symmetric because ICH and AIS constitute different scattering problems.

Overall, similar correlation patterns are observed for the two stroke types, and most of the adopted metrics are highly correlated. The highest correlations are observed between DSC, PCC, PSNR$_N$, AND CNR$_N$. In particular, DSC is highly correlated with all the other metrics, with coefficients ranging approximately from 0.84 to 1.00, except for its slightly lower correlation with BBM, $\rho = 0.79$. NRMS$_R$ and NRMS$_I$ are also highly correlated with each other, since both quantify reconstruction errors of complementary image components. On the other hand, BBM exhibits the lowest correlations, approximately between $\rho = 0.66$ and $\rho = 0.79$, indicating that boundary agreement of the reconstructed dielectric profile with respect to the expected one provides complementary information that other metrics can not capture. These results confirm the presence of substantial redundancy among several metrics and motivate the correlation-aware weighting adopted in the SWM.

IV. NUMERICAL RESULTS

A. Minimum Non-Redundant Antennas

To determine the minimum number of required antennas, N_a, in the multi-static array, the non-redundant sampling theory developed in [70], [71] for electromagnetic fields over bounded domains is adopted here. The minimum number of non-redundant samples must be slightly larger than N_0:

$$N_0 \approx \frac{2P}{\lambda_{\text{eff}}}, \tag{26}$$

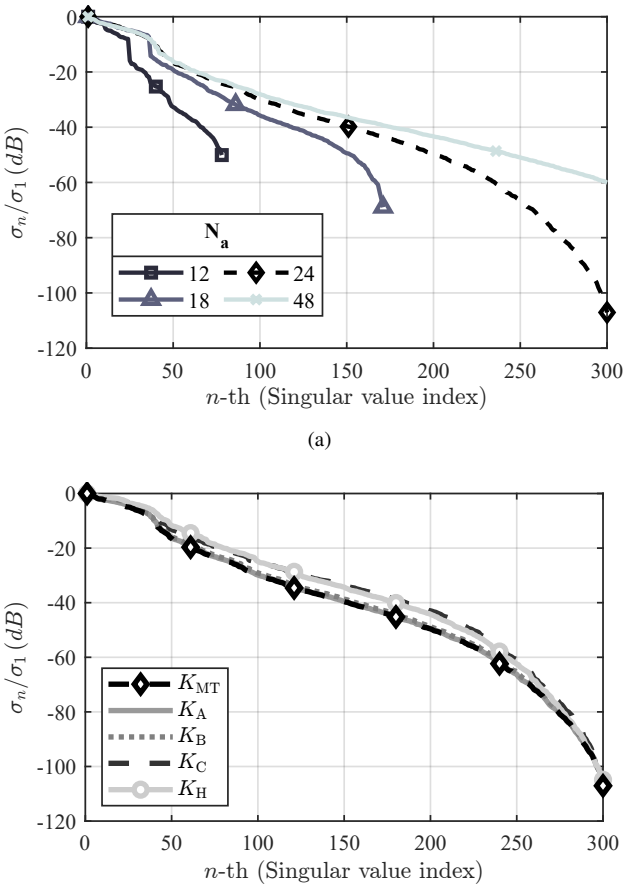

FIGURE 8. Singular values of different operators: (a) SV of MT operators with different numbers of antennas, and (b) all five different operators with 24 antennas.

which corresponds to a Nyquist-like sampling condition required to capture the spatial variations of the scattered field without aliasing, with P the perimeter of the observation domain, i.e., the perimeter of a head cross-section, and λ_{eff} the effective wavelength in the antenna host medium:

$$\lambda_{\text{eff}} = \frac{\lambda_0}{\sqrt{\bar{\varepsilon}_r}}, \qquad \lambda_0 = \frac{c}{f}, \tag{27}$$

where $\bar{\varepsilon}_r = 20$ represents the relative permittivity of the antenna matching medium, and $f = 1$ GHz the operating frequency.

The head perimeter P is computed from the twenty cross-section head models described in Sect. III-A. The mean value of P across all cases is 620 mm, with a standard deviation $\sigma_P = 22$ mm. Substituting the lower and upper bounds of the head perimeter into (26) yields a required number of degrees of freedom between 18 and 19 across the twenty head models. Since the number of samples should be chosen slightly larger than the estimated number of degrees of freedom, $N_a = 24$ antennas are selected. This choice introduces only marginal redundancy while providing additional robustness to measurement noise, as may occur in practical clinical scenarios. It is also supported by the metric-based results

This work is licensed under a Creative Commons Attribution-NonCommercial-NoDerivatives 4.0 License.
For more information, see https://creativecommons.org/licenses/by-nc-nd/4.0/

This article has been accepted for publication in IEEE Open Journal of Antennas and Propagation. This is the author's version which has not been fully edited and content may change prior to final publication. Citation information: DOI 10.1109/OJAP.2026.3724057

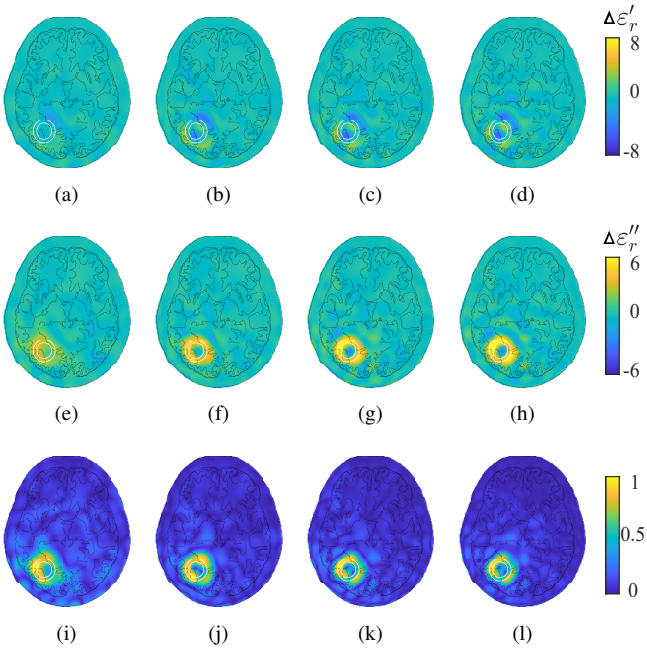

FIGURE 9. Impact of the number of antennas on the reconstructed dielectric contrast using the K_{MT} operator, for the 5 → 15 mL case. Top row: $\Delta\varepsilon_r'$, middle row: $\Delta\varepsilon_r''$, and bottom row: $|\Delta\varepsilon_{r,\mathrm{norm}}|$. Columns correspond to increasing number of antennas ($N_a = 12, 18, 24, 48$). For visualization, the head maps are displayed at 35% smaller visual scale than in Fig. 1.

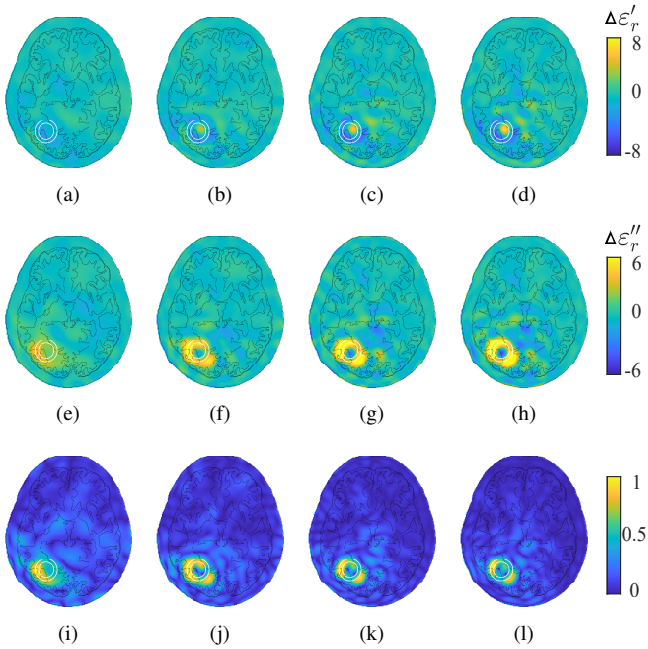

FIGURE 10. Impact of the number of antennas on the reconstructed dielectric contrast using the K_H operator, 5 → 15 mL case. Top row: $\Delta\varepsilon_r'$, middle row: $\Delta\varepsilon_r''$, and bottom row: $|\Delta\varepsilon_{r,\mathrm{norm}}|$. Columns correspond to increasing number of antennas ($N_a = 12, 18, 24, 48$). For visualization, the head maps are displayed at 35% smaller visual scale than in Fig. 1.

presented below, which indicate that $N_a = 24$ yields good reconstruction performance. Beyond a certain number of probes, additional ones do not proportionally improve image quality, indicating that only redundant information is added.

Figure 8a shows the singular values (SV) of K_{MT} vs N_a. Increasing the number of antennas N_{a} expands the spectrum of $[\mathbf{K}]$ and the overall decay becomes slower, and the tail singular values become smaller. This behavior indicates that additional antenna pairs yield highly correlated data and thus provide only marginally new information. As the number of antennas decreases, the singular values decay more sharply, meaning the operator quickly exhausts its independent spatial degrees of freedom. For each imaging kernel, the truncation index T is selected as the smallest index for which the cumulative singular-value energy reaches 99.99% of the total energy, as stated in Sec. II-B. The adopted cumulative-energy threshold represents a conservative compromise that retains the dominant information content of the imaging kernel and suppresses the low-energy singular components that are most sensitive to noise and modeling errors. In particular, for K_{MT} with N_a=24, the adopted cumulative-energy criterion yields $T = 150$. Figure 8b compares the singular values of the five inversion kernels for $N_a = 24$. All kernels behave similarly, with very similar curves and a slow decay, which suggests comparable information content and conditioning.

Hereafter, the retrieved reconstructions represent the real $\Delta\varepsilon_r'$ and imaginary $\Delta\varepsilon_r''$ parts of the complex relative permittivity contrast, $\Delta\varepsilon_r$. The color scales have been chosen using the expected dielectric contrast between the lesion and gray matter reported in Table 1, for $\Delta\varepsilon_r'$ from approximately -8 to 8, and -5 to 5 for ICH and AIS, respectively; and for $\Delta\varepsilon_r''$ from approximately -6 to 6, and -2 to 2 for ICH and AIS, respectively. Gray matter is selected as the representative surrounding brain tissue for defining consistent visualization ranges. Although the linear inversion based on the Born approximation and TSVD regularization does not provide fully quantitative estimates of the dielectric properties, the reconstructed dielectric profiles provide semi-quantitative information, including the spatial distribution, the approximate complex dielectric contrast, and the growing/shrinking, i.e., temporal evolution or transformation, of an ICH or AIS lesion.

Figures 9 and 10 report an SPH case $5 \rightarrow 15$ mL, which will be used for reference; other cases are reported in complementary materials. These show the impact of the number of antennas on the reconstructed dielectric contrast maps for the K_{MT} and K_{H} operators, respectively. In both cases, increasing N_a from 12 to 48 leads to a clear improvement in lesion localization, contrast, and spatial correspondence in the real, imaginary, and normalized-magnitude dielectric profiles. For $N_a = 12$, the reconstructions are contaminated by background artifacts, while $N_a = 18$ provides only a partial improvement. A marked transition is observed at $N_a = 24$, where the ICH stroke lesion becomes distinguishable with reduced background artifacts. The MWI reconstruction with $N_a = 48$ provides only marginal visual improvements, mainly in artifact reduction. This indicates a saturation effect:

This work is licensed under a Creative Commons Attribution-NonCommercial-NoDerivatives 4.0 License.
For more information, see https://creativecommons.org/licenses/by-nc-nd/4.0/

This article has been accepted for publication in IEEE Open Journal of Antennas and Propagation. This is the author's version which has not been fully edited and content may change prior to final publication. Citation information: DOI 10.1109/OJAP.2026.3724057

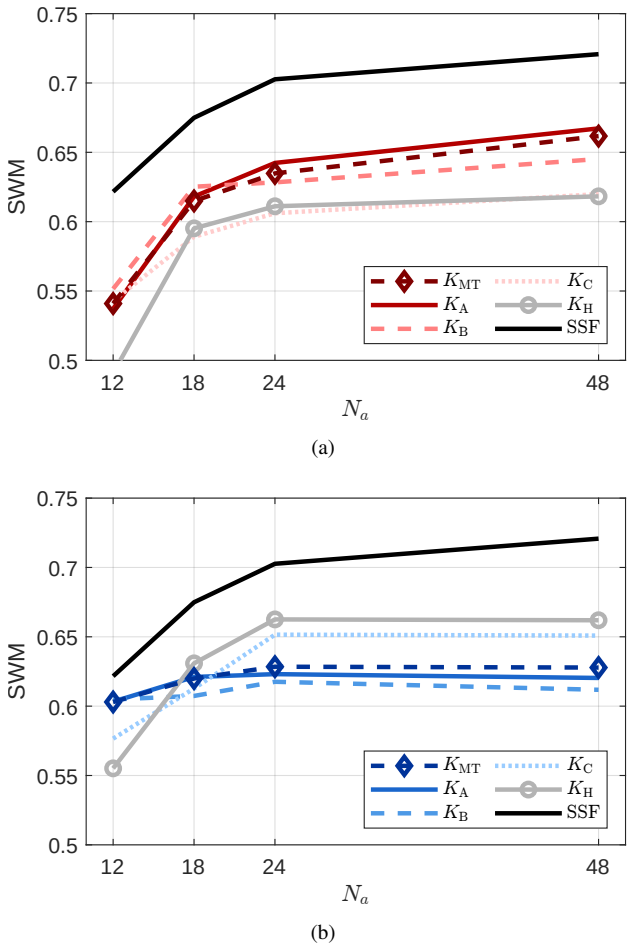

FIGURE 11. **Spearman-weighted metrics for a single patient (5→15 mL), C1 positions, using the SPH stroke model, as a function of the number of antennas. (a) ICH strokes, and (b) AIS strokes.**

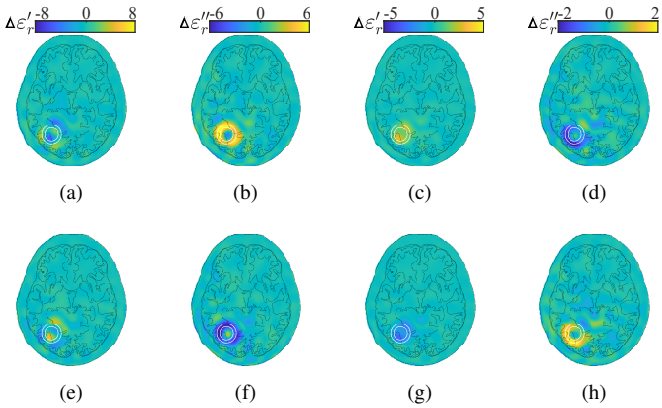

FIGURE 12. **Reconstruction comparison between ICH (columns 1-2) and AIS (columns 3-4) using 24 antennas and the K_{MT} operator. Top row: growing lesions (5→15 ml). Bottom row: shrinking lesions (5←15 ml). For visualization, the head maps are displayed at 35% smaller visual scale than in Fig. 1.**

most of the useful information is already captured with 24 antennas, which is also observed in Fig. 8a, where the singular values for $N_a = 24$ and $N_a = 48$ antennas have a common flattened behavior at around -40 dB, which corresponds to approximately the 99.99% of the total kernel energy. Similar results are found in [69] for a 3D case.

To quantitatively evaluate the visual assessment, the SWM is computed for the studied case and reported in Fig. 11 as a function of the number of antennas for all kernels and for both ICH and AIS cases. For all kernels, the best image quality is observed when increasing the number of antennas up to $N_a = 24$, whereas the improvement from 24 to 48 is much smaller. This trend is consistent across stroke types and confirms the visual observations from Figs. 9–10. Moreover, K_{MT}, K_{A}, and K_{B} generally achieve the highest SWM values, while K_{C} and K_{H} show lower performance for sparse antenna configurations and benefit more from increasing N_a. Overall, the SWM analysis confirms that $N_a = 24$ represents a good trade-off between reconstruction quality and system complexity. As a reference baseline, the shape spread function (SSF) is introduced to evaluate the reconstruction performance of a given imaging operator $\mathbf{K}$ for arbitrary dielectric contrast distributions under ideal conditions, i.e., in the absence of noise and background-model mismatch. SSF is defined as the orthogonal projection operator onto the truncated right-singular-vector subspace of the imaging kernel $\mathbf{K}$. When applied to a known dielectric contrast distribution $\Delta\varepsilon$, it yields the corresponding subspace-projected dielectric contrast $\Delta\varepsilon_{\mathrm{SSF}}$:

$$[\Delta\varepsilon_{\mathrm{SSF}}] = \sum_{n=1}^{T} ([v_n]^* [\Delta\varepsilon])\, [v_n], \tag{28}$$

where $[\cdot]^*$ indicates the conjugate transpose, $[v_n]$ the n-th right singular vectors of the discretized imaging operator, and T the truncation index. In Fig. 11, the SSF curve corresponds to the SWM obtained from $\Delta\varepsilon_{\mathrm{SSF}}$, where the ideal dielectric contrast distribution of the considered lesion is projected onto the truncated imaging kernel $\mathbf{K}_{MT}$; the contrast $\Delta\varepsilon$ is zero throughout the background and assumes the expected dielectric contrast only within the lesion region.

To include both growth and shrinkage cases, Fig. 12 extends the analysis by considering both ICH and AIS evolutions. This is particularly important for a monitoring approach, as it confirms that the adopted tomographic MWI algorithm correctly identifies whether the stroke extent is increasing (growing) or decreasing (shrinking) over time. This result shows that the sign and magnitude of the variation in $\Delta\varepsilon$ for the real and imaginary parts are correctly recovered. The normalized magnitude maps confirm that the lesion is correctly detected, regardless of whether its extent is expanding or shrinking.

B. Resolution and Tissue Variability

A parametric analysis of the spatial resolution of the prior input information together with the intra-tissue dielectric variability is presented in this section. For each of the five kernel operators, the pixel resolution is varied from 1 to 4 mm, while the scattering data $\Delta\mathbf{E}^{\mathrm{sc}}$ used for inversion is

This work is licensed under a Creative Commons Attribution-NonCommercial-NoDerivatives 4.0 License.
For more information, see https://creativecommons.org/licenses/by-nc-nd/4.0/

This article has been accepted for publication in IEEE Open Journal of Antennas and Propagation. This is the author's version which has not been fully edited and content may change prior to final publication. Citation information: DOI 10.1109/OJAP.2026.3724057

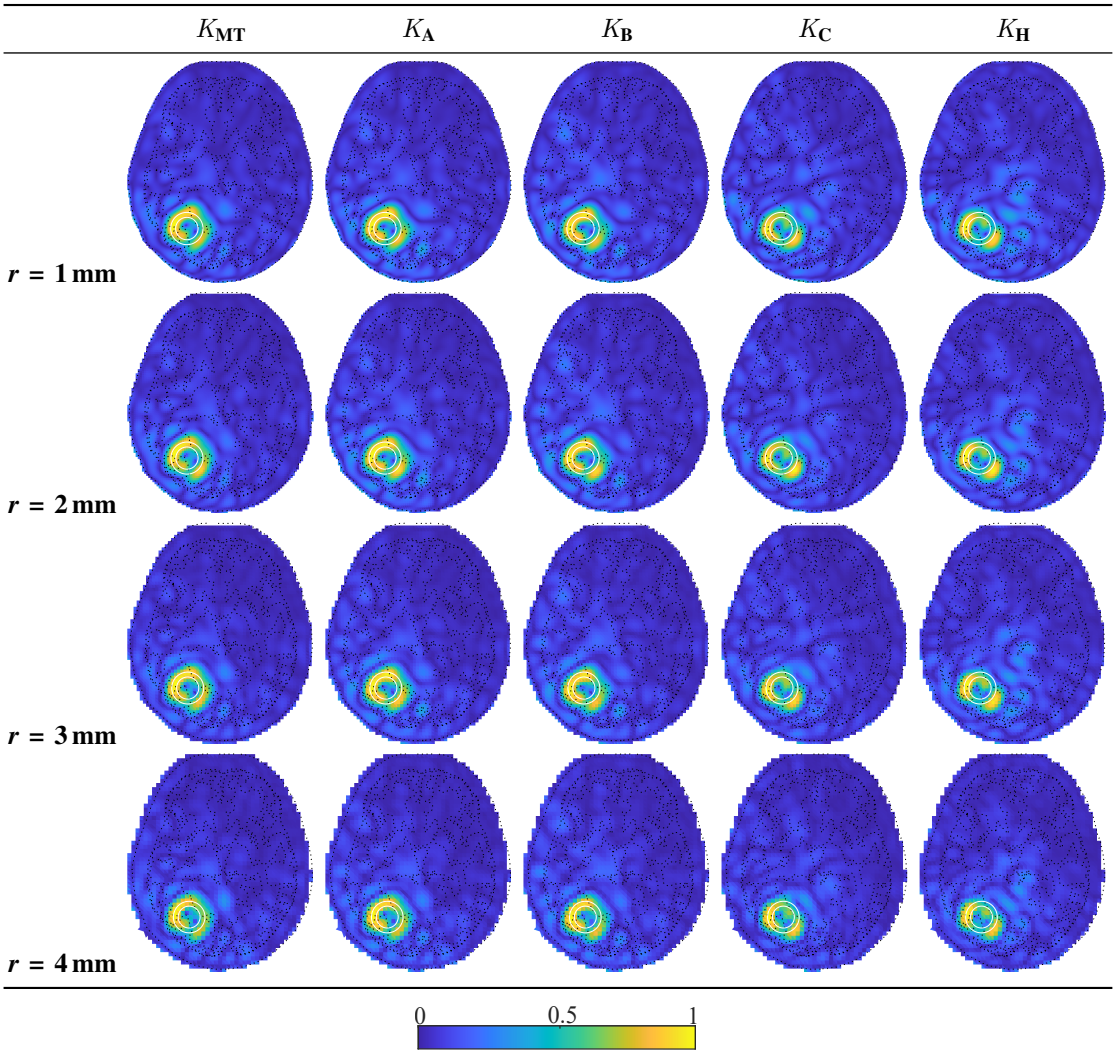

FIGURE 13. **Impact of the spatial resolution on the reconstructed dielectric contrast in 5 → 15 mL, ICH case, expressed as the normalized quantity $|\Delta\varepsilon_{r,\mathrm{norm}}|$. Columns correspond to different operators, while rows correspond to spatial resolutions of 1, 2, 3, and 4 mm. The number of antennas is fixed to $N_a = 24$. Head dimensions match Fig. 1.**

always computed at the reference resolution of $0.5\,\mathrm{mm}$, as described in Sect. III. The normalized differential contrast maps $|\Delta\varepsilon_{r,\mathrm{norm}}|$ of this analysis for a hemorrhagic monitoring scenario are shown in Fig. 13. Across all kernel operators and all input pixel resolutions, the evolving stroke region is spatially consistent with the expected lesion location. This preliminary observation suggests that a coarser pixel map of $4\,\mathrm{mm}$, directly linked to a coarser mesh and reduced computational resources for the forward EM simulations to build $\mathbf{K}$, achieves imaging results comparable to those obtained at $1\,\mathrm{mm}$ resolution. This finding is particularly relevant, as in three-dimensional (3-D) scenarios the computational cost of the forward solver scales significantly with mesh density, as well as for iterative methods.

To quantitatively support these findings, the SWM metric is calculated for each case and reported in Fig. 14. For both the ischemic and hemorrhagic cases, the resolution of the input pixel map has no significant impact on the imaging retrieval performance. A marginal decrease in metric values is observed at a resolution of 4 mm relative to 1 mm, but the values remain close to each other, suggesting that when patient-specific anatomical prior information is available, a high-resolution structural model is not strictly necessary for accurate stroke monitoring. Among the five kernels, K_{MT} achieves the best SWM, indicating that when no complete anatomical information is available, the overall quality of image retrieval is reduced. Conversely, K_{H} and K_{C}, the most structurally simplified kernels, have the lowest reconstruction accuracy across all resolutions and pathology types.

To further assess intra-tissue dielectric variability, different kernel operators under varying tissue heterogeneity are evaluated. In these kernels, the dielectric properties assigned to each tissue have a variance of 5% relative to the nominal values reported in Figs. 2a and 2b, thereby modeling a more realistic representation of the biological variability present in head tissues. The imaging performance with and without

This work is licensed under a Creative Commons Attribution-NonCommercial-NoDerivatives 4.0 License.
For more information, see https://creativecommons.org/licenses/by-nc-nd/4.0/

This article has been accepted for publication in IEEE Open Journal of Antennas and Propagation. This is the author's version which has not been fully edited and content may change prior to final publication. Citation information: DOI 10.1109/OJAP.2026.3724057

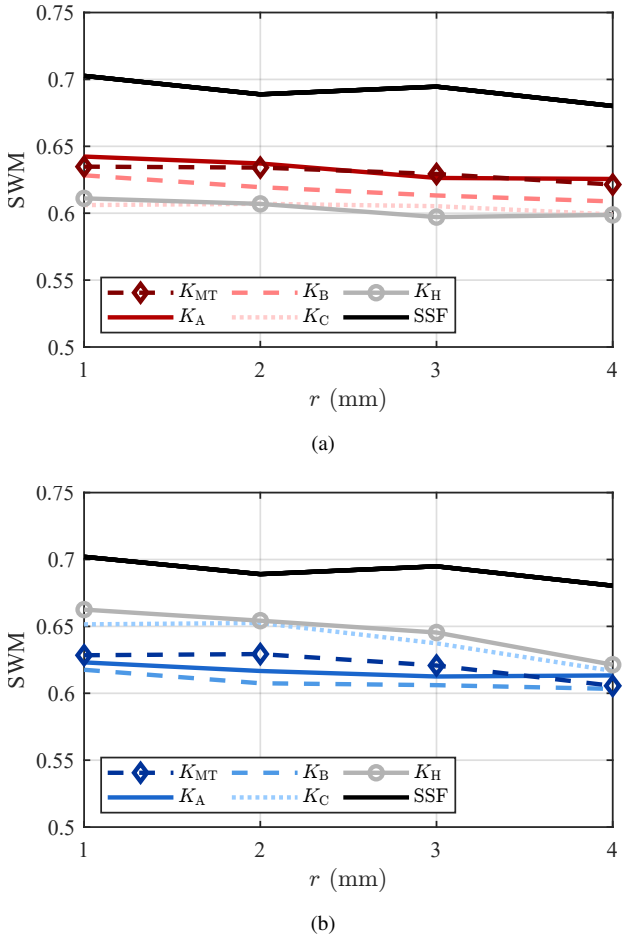

FIGURE 14. **Spearman-weighted metrics for a single patient (5→15 mL), C1 positions, using the SPH stroke model, as a function of resolution. (a) ICH strokes, and (b) AIS.**

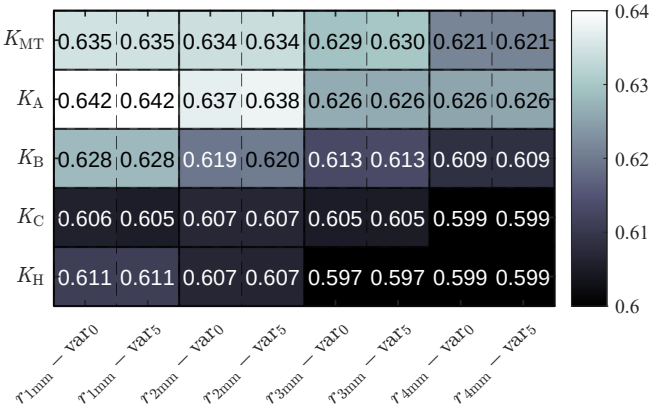

FIGURE 15. **Spearman-weighted metrics for a single patient (5→15 mL), C1 positions, using the ICH SPH stroke model, as a function of resolution and variance. Rows correspond to different operators, while columns represent resolutions, each shown for both the no-variance and variance cases.**

intra-tissue variability is compared in Fig. 15 for a single representative head model. The results indicate that, at 1 mm resolution, the six-tissue kernel K_{MT} achieves the highest performance independently of whether tissue heterogeneity is included, suggesting that intra-tissue dielectric variability does not contribute additional discriminative information in the imaging retrieval. Consistently, for all kernel operators and spatial resolutions, incorporating tissue heterogeneity does not report improvement in SWM, suggesting that dielectric variations within individual tissue regions are not crucial for achieving high-quality imaging.

These findings relax a modeling requirement of the kernel $\mathbf{K}$ and suggest that electromagnetic solvers assuming homogeneous surface or volume tissue properties can accurately reconstruct $\Delta\chi$, even when the data for inversion comes from a scenario with intra-tissue dielectric variability.

C. Extended Follow-up

After selecting $N_a = 24$ and a kernel resolution of 4 mm, the monitoring capability of the proposed approach is assessed by considering progressive lesion evolution scenarios. In particular, three volume transitions are analyzed, namely $0 \rightarrow 5$ mL, $5 \rightarrow 15$ mL, and $15 \rightarrow 25$ mL, which represent increasing levels of dielectric perturbation associated with stroke progression. The analysis is first reported for the SPH model, while the corresponding results for the CAP and ANM cases are provided in the supplementary materials.

Figure 16 shows the monitoring reconstructions obtained for the SPH case using the five kernel operators. For each operator, the real part $\Delta\varepsilon_r'$, the imaginary part $\Delta\varepsilon_r''$, and the normalized magnitude $|\Delta\varepsilon_{r,\mathrm{norm}}|$ are reported for the three considered monitoring transitions. Rows are arranged from the most anatomically detailed operator, the six-tissue model (K_{MT}, top), to the simplest structural operator (K_{H}, bottom).

In all cases, the reconstructed lesion remains localized within the expected stroke region, confirming that the system can track lesion evolution. The nominal permittivity values for gray and white matter ($\varepsilon_r' \approx 51$ and 43, respectively) increased to those characteristic of blood ($\varepsilon_r' \approx 62$). Consequently, the real part of the contrast in the evolving region, defined as $\Delta\varepsilon_r' = \varepsilon_r'(t_0) - \varepsilon_r'(t_1)$, is expected to be negative, which is observed consistently in all reconstructions. In addition, the imaginary part of the contrast, $\Delta\varepsilon_r''$, is expected to be positive, as observed in all reconstructions.

Among all kernels, K_{MT}, K_{A}, and K_{B} provide the reconstructions with the fewest background artifacts in the real, imaginary, and normalized magnitude of the retrieved dielectric contrast. By contrast, K_{C} and especially K_{H} show a more diffuse response and background artifacts, particularly for the smallest monitoring variation $0 \rightarrow 5$ mL. Nevertheless, even in these more challenging cases, the lesion position remains identifiable, indicating that the monitoring information is preserved across all operators, although with different levels of accuracy. A reduction in reconstruction performance is observed for the 15→25 mL transition. Although the local dielectric contrast remains unchanged, a larger spatial dielectric contrast increases the magnitude of the scattered field. Consequently, the latter becomes a more significant component of the total field, reducing the validity of the Born

This work is licensed under a Creative Commons Attribution-NonCommercial-NoDerivatives 4.0 License.
For more information, see https://creativecommons.org/licenses/by-nc-nd/4.0/

This article has been accepted for publication in IEEE Open Journal of Antennas and Propagation. This is the author's version which has not been fully edited and content may change prior to final publication. Citation information: DOI 10.1109/OJAP.2026.3724057

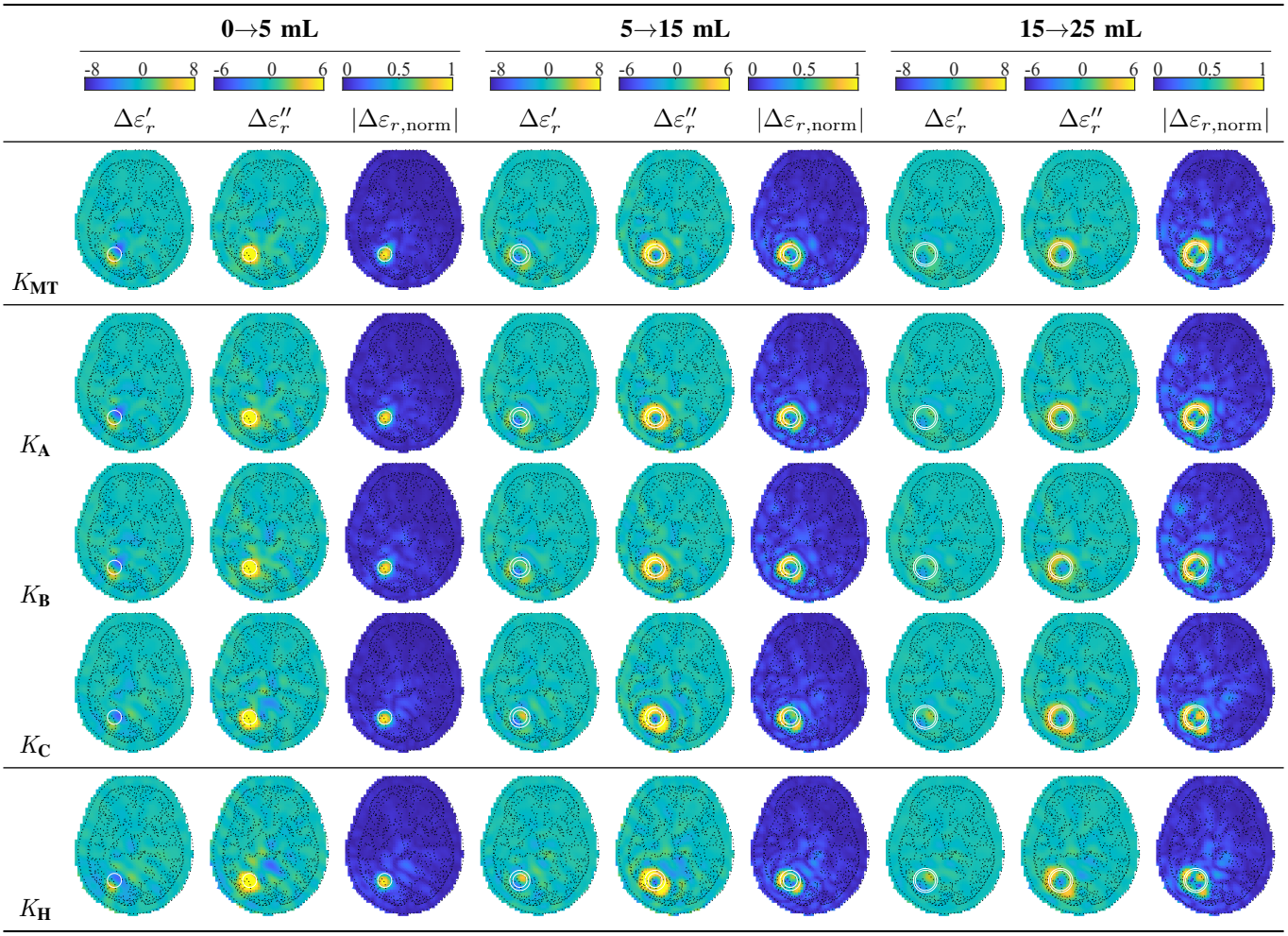

FIGURE 16. **Monitoring reconstruction comparison for different operators for the spherical stroke model. For visualization, the head maps are displayed at 35% smaller visual scale than in Fig. 1.**

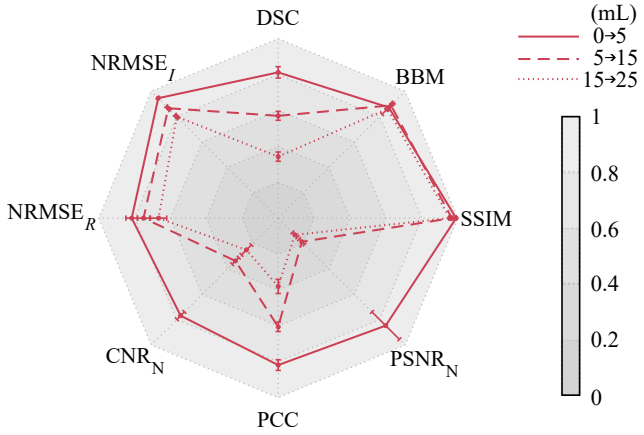

FIGURE 17. **Average metrics for all patients (monitoring), C1 positions, using the ICH SPH stroke model. Bars indicate the standard deviation across patients.**

approximation. Combined with the TSVD regularization, this explains the lower imaging performance metrics for the largest volume transition.

These qualitative results are quantitatively evaluated, and for each kernel operator, stroke pathology (ICH or AIS), and lesion location (C1, C2, and C3), the imaging quality metrics are computed across all twenty head models. Figure 17 shows, for each metric, the average value across the twenty head models along with the corresponding standard deviation of these twenty models. The low standard deviation suggests no substantial variation across all head model cases, demonstrating high consistency with respect to inter-subject anatomical variability. The supplementary materials include an extensive collection of plots for all evaluated cases.

A quantitative summary of these findings is shown in Fig. 18, which reports the SWM averaged across all patients for the SPH stroke morphology, considering the three lesion locations C1, C2, and C3, and the three monitoring intervals. The bar plots in Fig. 18 report a quantitative summary of the imaging performance metrics separately for the three monitoring cases, namely, $0 \rightarrow 5\,\mathrm{mL}$, $5 \rightarrow 15\,\mathrm{mL}$, and $15 \rightarrow 25\,\mathrm{mL}$. For all cases, K_{MT}, K_{A}, and K_{B} achieve the

This work is licensed under a Creative Commons Attribution-NonCommercial-NoDerivatives 4.0 License.
For more information, see https://creativecommons.org/licenses/by-nc-nd/4.0/

This article has been accepted for publication in IEEE Open Journal of Antennas and Propagation. This is the author's version which has not been fully edited and content may change prior to final publication. Citation information: DOI 10.1109/OJAP.2026.3724057

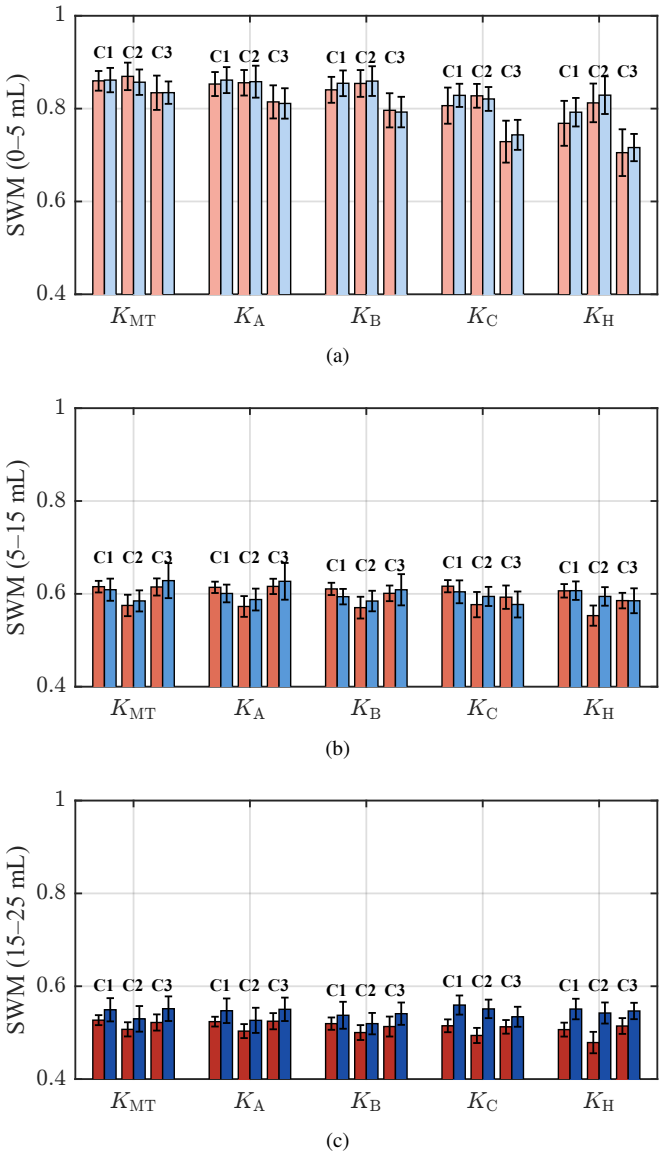

FIGURE 18. Spearman-weighted metrics computed across all patients for different monitoring scenarios: (a) 0→5 mL, (b) 5→15 mL, and (c) 15→25 mL. The color gradient encodes the dimensions of stroke variation, with red indicating ICH and blue indicating AIS. Results are shown for a spatial resolution of 4 mm, zero variance, and the SPH stroke model.

highest SWM values, with limited variations across the three lesion positions while K_{C} and K_{H} have lower metric values, in agreement with background artifacts in the reconstructions observed in Fig. 16. In addition, the quality of the reconstructions decreases as the monitoring interval moves from $0 \rightarrow 5\,\mathrm{mL}$ to $15 \rightarrow 25\,\mathrm{mL}$. This indicates that larger lesion areas may make image retrieval slightly more difficult using the kernels considered for this study. Nevertheless, despite this reduction, the overall retrieval performance of each kernel remains consistent across different lesion shapes, as reported in the supplementary materials. It is worth noting that the monitoring scenario $0 \rightarrow 5\,\mathrm{mL}$ achieves the best imaging performance metrics, regardless of lesion shape. However, as the lesion increases in size and develops more complex morphology, the reconstruction problem becomes more challenging, resulting in lower-quality imaging. Among all evaluated cases, the directional capsule-shaped lesion achieves the highest SWM values, as its morphology evolution is less challenging.

Overall, these results indicate that integrating prior anatomical information about the DoI reduces the inversion kernel's modeling error. Consequently, the MWI reconstructions exhibit fewer artifacts, a cleaner background, accurate lesion size, position, and boundary definition, good contrast between the lesion and surrounding tissues, and permittivity contrast values recovered with lower error. The qualitative MWI reconstructions help define the site and progression of a stroke lesion, while the quantitative data provide information on lesion shrinkage or growth and on the stroke type. Kernels that incorporate more prior anatomical information, such as K_{MT}, provide MWI reconstructions of superior quality, which is directly reflected in higher SWM values. Nonetheless, anatomically simplified inversion kernels, without detailed anatomical priors, can still identify lesions, albeit with lower precision. This implies that, although the best performance is achieved when accurate prior information is available, anatomically simplified kernels can still provide clinically meaningful insights when such detailed information is unavailable. Additionally, Table 6 reports the relative SWM percentage difference with respect to the K_{H} case, computed as $(\mathrm{SWM}_{K_{\mathrm{H}}} - \mathrm{SWM}_{K_{\mathrm{i}}})/\mathrm{SWM}_{K_{\mathrm{i}}}$, where $i \in \{\mathrm{MT}, \mathrm{A}, \mathrm{B}, \mathrm{C}\}$. It shows that there is an improvement of 4.03, 3.5, 2.76, and 1.06% for the K_{MT}, K_{A}, K_{B}, and K_{C} kernels, respectively. It highlights the added value of incorporating anatomical information about the head tissues into the monitoring problem.

D. Lesion-distorted Kernel

Up to this point, we have distorted the operator assuming $\mathbf{E}_i^{\mathrm{inc}}$ is a healthy head — *no lesion*. However, the prior information may also include the stroke-affected area at the onset, as part of the initial condition, or at the time of the initial clinical evaluation. Hence, to assess this point, we build a stroke-informed kernel using the initial onset as an incident scenario in (4). Specifically, and as an example, we consider a spherical ICH case in which the volume varies from $5\,\mathrm{mL}$ to $15\,\mathrm{mL}$, and from $15\,\mathrm{mL}$ to $25\,\mathrm{mL}$, while the operator is built using the case at $5\,\mathrm{mL}$. Then, we compare the effect of the stroke inclusion on both the multi-tissue and homogeneous cases, dubbing the new operators $K_{\mathrm{MT}_{\mathrm{stroke}}}$ and $K_{\mathrm{H}_{\mathrm{stroke}}}$, respectively.

Visually, both operators yield similar localization of the evolving lesion in the real, imaginary, and normalized-magnitude components of the reconstructed map, as can be noticed by comparing the maps in Fig. 19 with the corresponding maps in Fig. 16. To quantitatively evaluate the reconstructions, the imaging performance metrics for these cases are reported in Tables 4 and 5. In particular, the quan-

This work is licensed under a Creative Commons Attribution-NonCommercial-NoDerivatives 4.0 License.
For more information, see https://creativecommons.org/licenses/by-nc-nd/4.0/

This article has been accepted for publication in IEEE Open Journal of Antennas and Propagation. This is the author's version which has not been fully edited and content may change prior to final publication. Citation information: DOI 10.1109/OJAP.2026.3724057

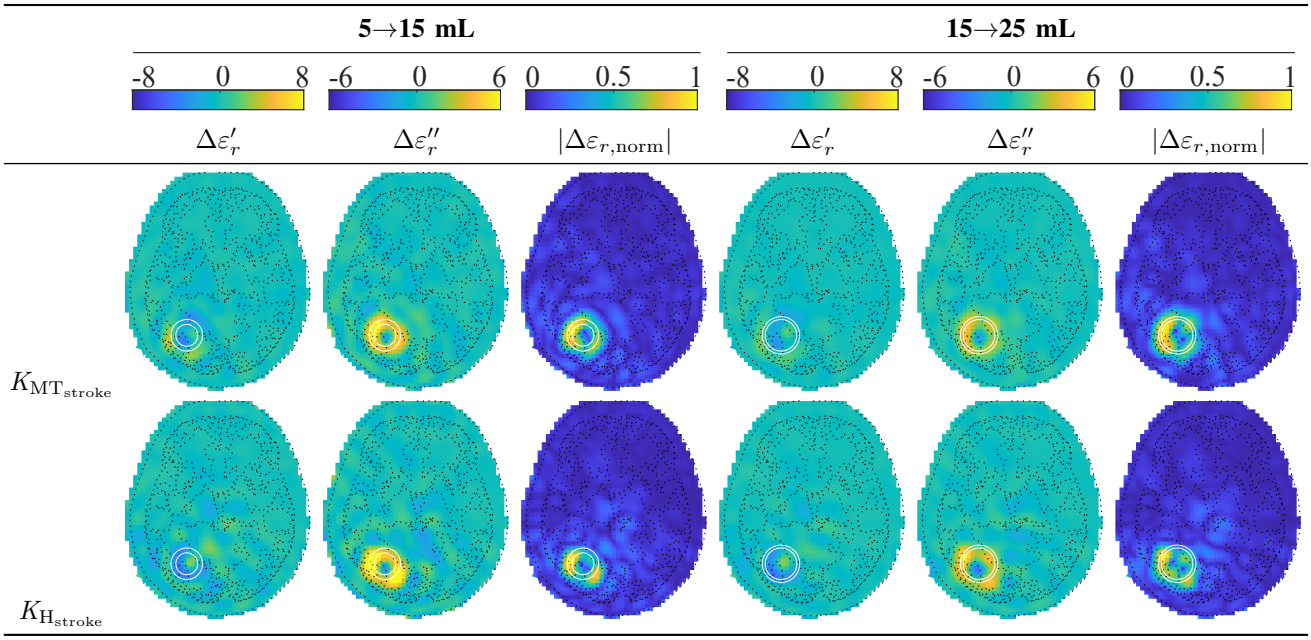

FIGURE 19. **Reconstruction comparison for one patient at position C3 using 24 antennas and a spatial resolution of 4 mm, for a spherical ICH stroke model, using a lesion-distorted kernel. For each operator, $K_{\mathrm{MT}_{\mathrm{stroke}}}$ and $K_{\mathrm{H}_{\mathrm{stroke}}}$, the first three columns refer to the 5→15 mL interval and the last three columns to the 15→25 mL interval. Columns show the reconstructed real permittivity ε_r', imaginary permittivity ε_r'', and normalized magnitude $|\Delta\varepsilon_{r,\mathrm{norm}}|$. Head dimensions match those in Fig. 1.**

TABLE 4. **Reconstruction metrics for 5→15 mL volume variation**

	DSC	BBM	SSIM	$\mathrm{PSNR_N}$	PCC	$\mathrm{CNR_N}$	NRMSE_R	NRMSE_I
No-lesion Kernel								
K_{MT}	0.53	0.84	0.97	0.18	0.55	0.32	0.69	0.83
K_{H}	0.36	0.83	0.97	0.16	0.35	0.28	0.77	0.86
Lesion-distorted Kernel								
K_{MT}	0.42	0.81	0.96	0.15	0.43	0.26	0.67	0.77
K_{H}	0.44	0.89	0.96	0.15	0.45	0.26	0.71	0.84

No-lesion kernel: $\mathrm{SWM_{MT}} = 0.63$, $\mathrm{SWM_H} = 0.59$.
Lesion-distorted kernel: $\mathrm{SWM_{MT}} = 0.57$, $\mathrm{SWM_H} = 0.60$.

TABLE 5. **Reconstruction metrics 15→25 mL volume variation**

	DSC	BBM	SSIM	$\mathrm{PSNR_N}$	PCC	$\mathrm{CNR_N}$	NRMSE_R	NRMSE_I
No-lesion Kernel								
K_{MT}	0.31	0.83	0.95	0.10	0.37	0.25	0.57	0.73
K_{H}	0.24	0.77	0.96	0.13	0.24	0.22	0.69	0.79
Lesion-distorted Kernel								
K_{MT}	0.24	0.81	0.95	0.10	0.27	0.21	0.59	0.73
K_{H}	0.29	0.76	0.96	0.12	0.32	0.22	0.72	0.80

No-lesion kernel: $\mathrm{SWM_{MT}} = 0.53$, $\mathrm{SWM_H} = 0.52$.
Lesion-distorted kernel: $\mathrm{SWM_{MT}} = 0.50$, $\mathrm{SWM_H} = 0.53$.

titative results indicate that the lesion-informed kernel has a slight degradation in SWM for the $K_{\mathrm{MT}_{\mathrm{stroke}}}$ kernel and only marginal differences for the $K_{\mathrm{H}_{\mathrm{stroke}}}$ kernel, in consistency with the reconstructions in Fig. 16 and Fig. 19. As outlined

TABLE 6. **Operators SWM performance relative to K_{H} [%]**

K_{MT}	K_{A}	K_{B}	K_{C}
4.80	4.21	3.41	1.17

in Sec. IV-C, the imaging kernel is constructed using a mesh resolution of 4 mm. At this resolution, the lesion geometry cannot be represented exactly, thereby introducing a modeling error, which can explain the slight degradation observed in the SWM metric relative to the standard kernel.

E. Noise Level Assessment

To assess the noise sensitivity of the reconstructed MWI images for inversion kernels at different SNR levels. The scattered fields $E_{t_0}^{\mathrm{sc}}$ and $E_{t_1}^{\mathrm{sc}}$ are independently contaminated with zero-mean additive white Gaussian noise at SNR values of 50, 75, and 100 dB. Figure 20 presents the outcomes for both ICH and AIS lesions for one of the twenty analyzed head models. The reported values are the mean of all stroke lesions across all inversion kernels, showing a systematic degradation as SNR decreases. Moreover, at low SNR, the ICH cases retain higher SWM values than the AIS cases, indicating that ICH lesion monitoring is comparatively more robust to noise. This highlights the importance of two essential aspects in real-world applications: first, a measurement environment with minimal electromagnetic interference, and second, an MWI system characterized by a low noise floor. In this case study, when the SNR is $\geq$ 75 dB, the image quality for both lesion types becomes similar.

This work is licensed under a Creative Commons Attribution-NonCommercial-NoDerivatives 4.0 License.
For more information, see https://creativecommons.org/licenses/by-nc-nd/4.0/

This article has been accepted for publication in IEEE Open Journal of Antennas and Propagation. This is the author's version which has not been fully edited and content may change prior to final publication. Citation information: DOI 10.1109/OJAP.2026.3724057

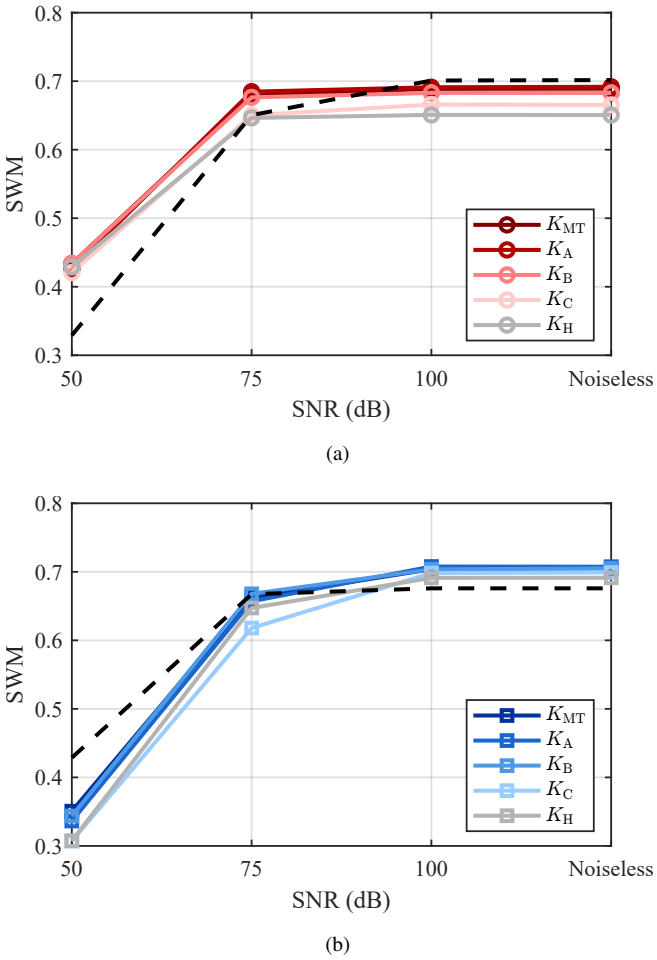

FIGURE 20. **Spearman-weighted metrics for a single patient for different kernels K, averaged across positions, models, and lesion sizes, using 24 antennas, 4 mm resolution, and zero variance, shown as a function of noise level: (a) ICH case and (b) AIS case. The black dashed lines in (a) and (b) indicate the SWM mean value of all kernels over all lesions for the AIS and ICH cases, respectively.**

V. CONCLUSION AND PERSPECTIVES

This work has presented a systematic investigation of the role of anatomical a priori information in the construction of inversion kernels for microwave imaging–based brain stroke monitoring. Using a large-scale numerical framework spanning a wide range of clinically relevant scenarios — covering different stroke types, morphologies, positions, antenna configurations, and model resolutions —we assessed, using multiple metrics, the impact of progressively simplified anatomical representations on the quality of the reconstructed images. The results consistently indicate that the reconstruction performance is mildly dependent on the level of structural detail embedded in the inversion kernel. While fully detailed multi-tissue models achieve the highest performance, simplified kernels that preserve only coarse anatomical information—or even a homogeneous representation of the head—can still reliably capture the main features of stroke evolution, including localization, extent, and temporal progression, in agreement with previously reported, 3-D cases [22], [53].

This trend is further confirmed by the proposed Spearman-weighted metric, which enables robust, non-redundant aggregation of multiple complementary imaging metrics. From a system design perspective, the analysis also shows and confirms that moderate system configurations, such as a limited number of antennas and coarse spatial discretizations, are sufficient to achieve stable and meaningful reconstructions, with only marginal gains obtained by increasing system complexity. These findings highlight an important practical implication: although beneficial, the availability of highly accurate, patient-specific anatomical information is not a strict requirement for effective microwave-based stroke monitoring. Overall, this study provides a general and reproducible methodological pathway to evaluate the distortion of anatomical prior kernels and supports the adoption of reduced-complexity inversion strategies in realistic clinical settings. This paves the way toward more robust, accessible, and portable monitoring systems, particularly in scenarios where conventional neuroimaging modalities are unavailable or impractical.

Possible next steps include extending the assessment to realistic 3-D configurations and studying antenna effects like polarization and alignment errors, evaluating different types of *a priori* information, and validating the results experimentally.

REFERENCES

[1] C. Origlia, D. O. Rodriguez-Duarte, J. A. Tobon Vasquez, J.-C. Bolomey, and F. Vipiana, "Review of microwave near-field sensing and imaging devices in medical applications," *Sensors*, vol. 24, no. 14, 2024.

[2] C. Yen, C.-L. Lin, and M.-C. Chiang, "Exploring the frontiers of neuroimaging: A review of recent advances in understanding brain functioning and disorders," *Life*, vol. 13, no. 7, 2023.

[3] J. Liu, L. Chen, H. Xiong, and Y. Han, "Review of microwave imaging algorithms for stroke detection," *Med. Biol. Eng. Comput.*, vol. 61, no. 10, pp. 2497–2510, 2023.

[4] N. K. Nikolova, *Introduction to microwave imaging*. Cambridge University Press, 2017.

[5] M. Pastorino, *Microwave imaging*. John Wiley & Sons, 2010.

[6] M. Bertero, P. Boccacci, and C. De Mol, *Introduction to inverse problems in imaging*. CRC press, 2021.

[7] A. H. Golnabi, P. M. Meaney, and K. D. Paulsen, "Tomographic microwave imaging with incorporated prior spatial information," *IEEE Trans. Microw. Theory Techn.*, vol. 61, no. 5, pp. 2129–2136, 2013.

[8] N. Abdollahi, D. Kurrant, P. Mojabi, M. Omer, E. Fear, and J. LoVetri, "Incorporation of ultrasonic prior information for improving quantitative microwave imaging of breast," *IEEE J. Multiscale Multiphys. Comput. Techn.*, vol. 4, pp. 98–110, 2019.

[9] D. Kurrant, A. Baran, J. LoVetri, and E. Fear, "Integrating prior information into microwave tomography part 1: Impact of detail on image quality," *Med. Phys.*, vol. 44, no. 12, pp. 6461–6481, 2017.

[10] D. Kurrant, E. Fear, A. Baran, and J. LoVetri, "Integrating prior information into microwave tomography part 2: Impact of errors in prior information on microwave tomography image quality," *Med. Phys.*, vol. 44, no. 12, pp. 6482–6503, 2017.

[11] M. Alkhodari, A. Zakaria, and N. Qaddoumi, "Using prior information to enhance microwave tomography images in bone health assessment," *Biomed. Eng. Online*, vol. 21, no. 1, p. 8, 2022.

[12] D. Ninković, A. Kovačević, B. Kolundžija, L. Crocco, and M. N. Stevanović, "Patient-specific background model estimation for effective

This work is licensed under a Creative Commons Attribution-NonCommercial-NoDerivatives 4.0 License.
For more information, see https://creativecommons.org/licenses/by-nc-nd/4.0/

This article has been accepted for publication in IEEE Open Journal of Antennas and Propagation. This is the author's version which has not been fully edited and content may change prior to final publication. Citation information: DOI 10.1109/OJAP.2026.3724057

brain stroke microwave imaging," *IEEE Trans. Med. Imag.*, pp. 1–1, 2026.

[13] Z. Gong, Y. Chen, Y. Ding, and H. Zhang, "Perspective: Microwave medical imaging using space-time-frequency a priori knowledge for health monitoring," *IEEE J. Electromagn., RF, Microw. Med. Biol.*, vol. 8, no. 1, pp. 2–14, 2024.

[14] M. L. Prust, A. Mbonde, C. Rubinos, G. S. Shrestha, M. Komolafe, D. Saylor, and H. S. Mangat, "Providing neurocritical care in resource-limited settings: challenges and opportunities," *Neurocrit. Care*, vol. 37, no. 2, pp. 583–592, 2022.

[15] F. Xue, L. Guo, A. Bialkowski, and A. M. Abbosh, "Integrated boundary-overlap-size metric for local assessment of deep learning methods in medical microwave imaging," *IEEE J. Electromagn., RF, Microw. Med. Biol.*, vol. 9, no. 2, pp. 229–239, 2025.

[16] Z. Wang, A. Bovik, H. Sheikh, and E. Simoncelli, "Image quality assessment: from error visibility to structural similarity," *IEEE Trans. Image Process.*, vol. 13, no. 4, pp. 600–612, 2004.

[17] K. H. Zou, S. K. Warfield, A. Bharatha, C. M. Tempany, M. R. Kaus, S. J. Haker, W. M. Wells III, F. A. Jolesz, and R. Kikinis, "Statistical validation of image segmentation quality based on a spatial overlap index1: scientific reports," *Acad. Radiol.*, vol. 11, no. 2, pp. 178–189, 2004.

[18] B. R. Lavoie, J. Bourqui, E. C. Fear, and M. Okoniewski, "Metrics for assessing the similarity of microwave breast imaging scans of healthy volunteers," *IEEE Trans. Med. Imag.*, vol. 37, no. 8, pp. 1788–1798, 2018.

[19] D. O'Loughlin, B. L. Oliveira, M. A. Elahi, M. Glavin, E. Jones, M. Popović, and M. O'Halloran, "Parameter search algorithms for microwave radar-based breast imaging: Focal quality metrics as fitness functions," *Sensors*, vol. 17, no. 12, p. 2823, 2017.

[20] H. V. Lopes, D. M. Godinho, and R. C. Conceição, "Quantitative evaluation of repeatability in medical microwave imaging: A systematic review," *IEEE Access*, vol. 13, pp. 202 524–202 538, 2025.

[21] D. O. Rodriguez-Duarte, C. Origlia, J. A. T. Vasquez, R. Scapaticci, L. Crocco, and F. Vipiana, "Experimental assessment of real-time brain stroke monitoring via a microwave imaging scanner," *IEEE Open J. Antennas Propag.*, vol. 3, pp. 824–835, 2022.

[22] A. R. Masaquiza-Caiza, M. Gugliermino, D. O. Rodriguez-Duarte, and F. Vipiana, "Microwave imaging evaluation of prior structural information on the inversion-kernel building apply to a brain stroke monitoring scenario," in *Proc. Int. Conf. Electromagn. Adv. Appl. (ICEAA)*, 2025, pp. 1070–1071.

[23] A. S. Beaverstone, D. S. Shumakov, and N. K. Nikolova, "Frequency-domain integral equations of scattering for complex scalar responses," *IEEE Trans. Microw. Theory Techn.*, vol. 65, no. 4, pp. 1120–1132, 2017.

[24] M. Haynes, J. Stang, and M. Moghaddam, "Real-time microwave imaging of differential temperature for thermal therapy monitoring," *IEEE Trans. Biomed. Eng.*, vol. 61, no. 6, pp. 1787–1797, 2014.

[25] R. Scapaticci, O. M. Bucci, I. Catapano, and L. Crocco, "Differential microwave imaging for brain stroke followup," *Int. J. Antennas Propag.*, vol. 2014, no. 1, p. 312528, 2014.

[26] I. Merunka, A. Massa, D. Vrba, O. Fiser, M. Salucci, and J. Vrba, "Microwave tomography system for methodical testing of human brain stroke detection approaches," *Int. J. Antennas Propag.*, vol. 2019, no. 1, p. 4074862, 2019.

[27] D. Tajik, F. Foroutan, D. S. Shumakov, A. D. Pitcher, and N. K. Nikolova, "Real-time microwave imaging of a compressed breast phantom with planar scanning," *IEEE J. Electromagn., RF, Microw. Med. Biol.*, vol. 2, no. 3, pp. 154–162, 2018.

[28] G. H. Golub and C. F. Van Loan, *Matrix computations*. JHU press, 2013.

[29] R. A. Horn and C. R. Johnson, *Matrix analysis*. Cambridge university press, 2012.

[30] M. Osadebey, M. Pedersen, D. Arnold, and K. Wendel-Mitoraj, "Image Quality Evaluation in Clinical Research: A Case Study on Brain and Cardiac MRI Images in Multi-Center Clinical Trials," *IEEE J. Transl. Eng. Health Med.*, vol. 6, pp. 1–15, 2018.

[31] L. Lenchik, L. Heacock, A. A. Weaver, R. D. Boutin, T. S. Cook, J. Itri, C. G. Filippi, R. P. Gullapalli, J. Lee, M. Zagurovskaya *et al.*, "Automated segmentation of tissues using CT and MRI: a systematic review," *Acad. Radiol.*, vol. 26, no. 12, pp. 1695–1706, 2019.

[32] J. De Zaeytijd and A. Franchois, "Three-dimensional quantitative microwave imaging from measured data with multiplicative smoothing and value picking regularization," *Inverse Probl.*, vol. 25, no. 2, p. 024004, feb 2009.

[33] N. K. Nikolova, "Performance metrics in imaging," in *Introduction to Microwave Imaging*. Cambridge University Press, 2017, pp. 266–289.

[34] L. R. Dice, "Measures of the amount of ecologic association between species," *Ecology*, vol. 26, no. 3, pp. 297–302, 1945.

[35] C. M. Butterworth, P. Mojabi, and E. C. Fear, "Quantifying consistency of microwave breast imaging: Laser scanning for assessing breast volume and shape," *IEEE J. Electromagn., RF, Microw. Med. Biol.*, vol. 9, no. 3, pp. 335–343, 2025.

[36] D. Huttenlocher, G. Klanderman, and W. Rucklidge, "Comparing images using the hausdorff distance," *IEEE Trans. Pattern Anal. Mach. Intell.*, vol. 15, no. 9, pp. 850–863, 1993.

[37] M.-P. Dubuisson and A. Jain, "A modified hausdorff distance for object matching," in *Proc. 12th Int. Conf. Pattern Recognit. (ICPR)*, vol. 1, 1994, pp. 566–568 vol.1.

[38] E. Porter, M. Coates, and M. Popović, "An early clinical study of time-domain microwave radar for breast health monitoring," *IEEE Trans. Biomed. Eng.*, vol. 63, no. 3, pp. 530–539, 2016.

[39] R. Guo, Z. Lin, J. Xin, M. Li, F. Yang, S. Xu, and A. Abubakar, "Three dimensional microwave data inversion in feature space for stroke imaging," *IEEE Trans. Med. Imag.*, vol. 43, no. 4, pp. 1365–1376, 2024.

[40] B. Sohani, J. Puttock, B. Khalesi, N. Ghavami, M. Ghavami, S. Dudley, and G. Tiberi, "Developing artefact removal algorithms to process data from a microwave imaging device for haemorrhagic stroke detection," *Sensors*, vol. 20, no. 19, p. 5545, 2020.

[41] A. Rodriguez-Molares, O. M. H. Rindal, J. D'hooge, S.-E. Måsøy, A. Austeng, M. A. Lediju Bell, and H. Torp, "The Generalized Contrast-to-Noise Ratio: A Formal Definition for Lesion Detectability," *IEEE Trans. Ultrason., Ferroelectr., Freq. Control*, vol. 67, no. 4, pp. 745–759, 2020.

[42] D. R. I. M. Setiadi, "PSNR vs SSIM: imperceptibility quality assessment for image steganography," *Multimedia Tools Appl.*, vol. 80, no. 6, pp. 8423–8444, 2021.

[43] F. Xue, L. Guo, A. Bialkowski, and A. M. Abbosh, "Transfer deep learning for dielectric profile reconstruction in microwave medical imaging," *IEEE J. Electromagn., RF, Microw. Med. Biol.*, vol. 8, no. 4, pp. 344–354, 2024.

[44] L. Wang, "Multi-frequency holographic microwave imaging for breast lesion detection," *IEEE Access*, vol. 7, pp. 83 984–83 993, 2019.

[45] K. Smith, J. Bourqui, D. Garrett, S. Zarnke, M. Owjimehr, D. Deutscher, T. Fung, and E. Fear, "Microwave imaging of the breast: Consistency of measurements over time," *IEEE J. Electromagn., RF, Microw. Med. Biol.*, vol. 6, no. 1, pp. 61–67, 2022.

[46] B. Amin, A. Shahzad, M. O'Halloran, and M. A. Elahi, "Microwave bone imaging: A preliminary investigation on numerical bone phantoms for bone health monitoring," *Sensors*, vol. 20, no. 21, p. 6320, 2020.

[47] M. Borghouts, M. Ambrosanio, S. Franceschini, M. M. Autorino, V. Pascazio, and F. Baselice, "Microwave breast sensing via deep learning for tumor spatial localization by probability maps," *Bioengineering*, vol. 10, no. 10, p. 1153, 2023.

[48] B. Aubert-Broche, M. Griffin, G. Pike, A. Evans, and D. Collins, "Twenty new digital brain phantoms for creation of validation image data bases," *IEEE Trans. Med. Imag.*, vol. 25, no. 11, pp. 1410–1416, 2006.

[49] "An internet resource for the calculation of the dielectric properties of body tissues in the frequency range 10 Hz - 100 GHz," Available at http://niremf.ifac.cnr.it/tissprop/htmlclie/htmlclie.php.

[50] S. Y. Semenov and D. R. Corfield, "Microwave tomography for brain imaging: Feasibility assessment for stroke detection," *Int. J. Antennas Propag.*, vol. 2008, no. 1, p. 254830, 2008.

[51] O. Karadima, P. Lu, I. Sotiriou, and P. Kosmas, "Experimental Validation of the DBIM-TwIST Algorithm for Brain Stroke Detection and Differentiation Using a Multi-Layered Anatomically Complex Head Phantom," *IEEE Open J. Antennas Propag.*, vol. 3, pp. 274–286, 2022.

[52] D. O. Rodriguez-Duarte, J. A. Tobon Vasquez, S. De Luque Arias, R. Scapaticci, L. Crocco, and F. Vipiana, "A portable microwave scanner for brain stroke monitoring: Design, implementation and experimental validation," in *Proc. 16th Eur. Conf. Antennas Propag. (EuCAP)*, 2022, pp. 1–5.

[53] D. O. Rodriguez-Duarte, J. A. Tobón Vasquez, C. Origlia, R. Scapaticci, G. Turvani, M. R. Casu, L. Crocco, and F. Vipiana, *Towards a*

This work is licensed under a Creative Commons Attribution-NonCommercial-NoDerivatives 4.0 License.
For more information, see https://creativecommons.org/licenses/by-nc-nd/4.0/

This article has been accepted for publication in IEEE Open Journal of Antennas and Propagation. This is the author's version which has not been fully edited and content may change prior to final publication. Citation information: DOI 10.1109/OJAP.2026.3724057

Microwave Imaging Device for Cerebrovascular Diseases Monitoring: from Numerical Modeling to Experimental Testing. Cham: Springer International Publishing, 2023, pp. 203–233.

[54] D. Kuriakose and Z. Xiao, "Pathophysiology and treatment of stroke: present status and future perspectives," *Int. J. Mol. Sci.*, vol. 21, no. 20, p. 7609, 2020.

[55] Z. Ahmed, F. Chaudhary, and D. K. Agrawal, "Epidemiology, pathophysiology, and current treatment strategies in stroke," *Cardiol. Cardiovasc. Med.*, vol. 8, no. 4, p. 389, 2024.

[56] R. Scapaticci, L. Di Donato, I. Catapano, and L. Crocco, "A feasibility study on microwave imaging for brain stroke monitoring," *Prog. Electromagn. Res. B*, vol. 40, pp. 305–324, 2012.

[57] I. Bisio, A. Fedeli, F. Lavagetto, M. Pastorino, A. Randazzo, A. Sciarrone, and E. Tavanti, "A numerical study concerning brain stroke detection by microwave imaging systems," *Multimedia Tools Appl.*, vol. 77, no. 8, pp. 9341–9363, 2018.

[58] I. Despotović, B. Goossens, and W. Philips, "MRI segmentation of the human brain: challenges, methods, and applications," *Comput. Math. Methods Med.*, vol. 2015, no. 1, p. 450341, 2015.

[59] R. Ranjbarzadeh, A. Caputo, E. B. Tirkolaee, S. Jafarzadeh Ghoushchi, and M. Bendechache, "Brain tumor segmentation of MRI images: A comprehensive review on the application of artificial intelligence tools," *Comput. Biol. Med.*, vol. 152, p. 106405, 2023.

[60] Y. Zhang, Z. Shen, and R. Jiao, "Segment anything model for medical image segmentation: Current applications and future directions," *Comput. Biol. Med.*, vol. 171, p. 108238, 2024.

[61] N. Sharma and L. M. Aggarwal, "Automated medical image segmentation techniques," *J. Med. Phys.*, vol. 35, no. 1, pp. 3–14, 2010.

[62] S. C. Van De Leemput, M. Meijs, A. Patel, F. J. A. Meijer, B. Van Ginneken, and R. Manniesing, "Multiclass Brain Tissue Segmentation in 4D CT Using Convolutional Neural Networks," *IEEE Access*, vol. 7, pp. 51 557–51 569, 2019.

[63] S. Sangui, T. Iqbal, P. C. Chandra, S. K. Ghosh, and A. Ghosh, "3D MRI Segmentation using U-Net Architecture for the detection of Brain Tumor," *Procedia Comput. Sci.*, vol. 218, pp. 542–553, 2023.

[64] L. Dora, S. Agrawal, R. Panda, and A. Abraham, "State-of-the-art methods for brain tissue segmentation: A review," *IEEE Rev. Biomed. Eng.*, vol. 10, pp. 235–249, 2017.

[65] W. W. Moses, "Fundamental limits of spatial resolution in PET," *Nucl. Instrum. Methods Phys. Res. A*, vol. 648, pp. S236–S240, 2011.

[66] K. S. Nayak, Y. Lim, A. E. Campbell-Washburn, and J. Steeden, "Real-time magnetic resonance imaging," *J. Magn. Reson. Imaging*, vol. 55, no. 1, pp. 81–99, 2022.

[67] A. J. Sorby-Adams, J. Guo, P. Laso, J. E. Kirsch, J. Zabinska, A.-L. Garcia Guarniz, P. W. Schaefer, S. Payabvash, A. de Havenon, M. S. Rosen *et al.*, "Portable, low-field magnetic resonance imaging for evaluation of Alzheimer's disease," *Nat. Commun.*, vol. 15, no. 1, p. 10488, 2024.

[68] M. Slaney, A. Kak, and L. Larsen, "Limitations of imaging with first-order diffraction tomography," *IEEE Trans. Microw. Theory Techn.*, vol. 32, no. 8, pp. 860–874, 1984.

[69] R. Scapaticci, J. Tobon, G. Bellizzi, F. Vipiana, and L. Crocco, "Design and numerical characterization of a low-complexity microwave device for brain stroke monitoring," *IEEE Trans. Antennas Propag.*, vol. 66, no. 12, pp. 7328–7338, 2018.

[70] O. Bucci and G. Franceschetti, "On the degrees of freedom of scattered fields," *IEEE Trans. Antennas Propag.*, vol. 37, no. 7, pp. 918–926, 1989.

[71] O. Bucci, C. Gennarelli, and C. Savarese, "Representation of electromagnetic fields over arbitrary surfaces by a finite and nonredundant number of samples," *IEEE Trans. Antennas Propag.*, vol. 46, no. 3, pp. 351–359, 1998.



A. RAMIRO MASAQUIZA-CAIZA A. Ramiro Masaquiza-Caiza (Member, IEEE) received the B.Sc. degree in electronics, telecommunications and networking from Escuela Superior Politecnica de Chimborazo, Riobamba, Ecuador in 2021 and the M.Sc. in telecommunication engineering, smart sensing, computing and networking from the University of Calabria, Cosenza, Italy in 2024. He is currently pursuing his PhD in electrical, electronics and communications engineering at Politecnico di Torino, Italy. His current research interests include antenna theory and design, inverse scattering problems, and microwave sensing and imaging for biomedical applications.



DAVID O. RODRIGUEZ-DUARTE David O. Rodriguez-Duarte (Member, IEEE) received the B.Sc. and M.Sc. degrees in electronic engineering from Universidad Nacional de Colombia, Bogota, Colombia, in 2013 and 2018, respectively, and the Ph.D. degree from the Department of Electronics and Telecommunications, Politecnico di Torino, Turin, Italy, in 2022, where he is currently Assistant Professor, focusing on applied electromagnetics to biomedical and agro-industrial problems. He is a 2026 IEEE AP-S YP Ambassador, and the training leader on Antenna systems for the European Project "Bone, Brain, Breast and Axillary Medical Microwave Imaging (3BATwin)", and pre-clinical testing leader in the Interreg European Project "MedWaveImage, Microwave imaging technology transfer to innovate the medical sector. He is technical programme chair of the first "International Conference on Medical Microwave Imaging Applications (ICMWIA, 2026)," and has been convener of the sessions "Advancements on Electromagnetic-based Medical Techniques and Devices" at the Latin American Conference on Antennas and Propagation (LACAP2024), and "Advances in Electromagnetic Diagnostics, Therapeutics and Biomedical Sensors" at the European Conference on Antennas and Propagation (EuCAP2023)". He has been a Marie Sklodowska-Curie Early-Stage-Research Fellow in the European project EMERALD, 2018-21, visiting research at Keysight Technologies GmbH (Austria), iLumens-Health Simulation Center (France), King's College London (UK), WIPL-D d.o.o.(Serbia). In 2017, he was a visiting researcher at the University of British Columbia, Okanagan, BC, Canada, funded by the Emerging Leaders in the Americas Program, ELAP. He received the Individual Grant for Young Researcher to pursue high-risk, high-gain research in 2025, ranked 1st/70, funded by Politecnico di Torino and Fondazione Compagnia di San Paolo. He received the IEEE APS Postdoctoral Fellowship in 2022. He was awarded the best undergraduate thesis of the electronics department in 2013, the Second Prize in the Student Paper Competition in the 2021 URSI GASS, the AP-S Tapan Sarkar Best Student Paper in 2021 IEEE CAMA, the C. J. Reddy Travel Grant for Graduate Students in IEEE AP-S/URSI 2021, the best Propagation Paper finalist in EuCAP2022, the Young Scientist Award (YSA) at the URSI AT-AP-RASC in 2022, and a finalist for YSA at the 2023 URSI Spain National Symposium.



MARTINA GUGLIERMINO Martina Guglielmino (Member, IEEE) received the B.S. and M.S. degrees in biomedical engineering from the Politecnico di Torino, Turin, Italy, in 2020 and 2022, respectively. Her M.S. thesis focused on the realization and testing of a multi-tissue phantom for microwave sensing applications. From January to November 2023, she was a Research Assistant with the Department of Electronics and Telecommunications, Politecnico di Torino, where she worked on the development of synthetic tissues for imaging and electromagnetic sensing applications. She is currently pursuing the Ph.D. degree in electrical, electronics and communications engineering at the Politecnico di Torino. Her research activity focuses on portable microwave systems for brain stroke monitoring, including dielectric characterization, antenna design, phantom development, and microwave measurements. She received the IEEE Antennas and Propagation Society

This work is licensed under a Creative Commons Attribution-NonCommercial-NoDerivatives 4.0 License.

For more information, see https://creativecommons.org/licenses/by-nc-nd/4.0/

This article has been accepted for publication in IEEE Open Journal of Antennas and Propagation. This is the author's version which has not been fully edited and content may change prior to final publication. Citation information: DOI 10.1109/OJAP.2026.3724057

Mojgan Daneshmand Grant for Women in 2024, the European Microwave Week Student Grant in 2024, and the Women in Radio Science Grant for EuCAP 2025.



VALERIA MARIANO Valeria Mariano (Member, IEEE) received the bachelor's degree in biomedical engineering in 2017 and the master's degree (summa cum laude) in biomedical engineering in 2019 with a specialization in medical instrumentation from the Politecnico di Torino, Torino, Italy, where she received the Ph.D. degree (summa cum laude) in electronics and telecommunication engineering in 2023. In 2022, she was a Visiting Researcher with the University of Manitoba, Winnipeg, MB, Canada. She is currently a Postdoc Researcher with Politecnico di Torino. Her research interests include data processing and software implementation of deterministic algorithms and machine learning-based algorithms for the development of a microwave imaging device for brain stroke diagnosis. She was the recipient of the TICRA Travel Grant at the International Symposium on Antennas and Propagation in 2022, and the Young Scientist Award at the URSI Atlantic Radio Science Meeting in 2024.



FRANCESCA VIPIANA Francesca Vipiana (Senior Member, IEEE) received the Laurea and Ph.D. degrees in electronic engineering from the Politecnico di Torino, Torino, Italy, in 2000 and 2004, respectively, with doctoral research carried out partly at the European Space Research Technology Center, Noordwijk, The Netherlands. From 2005 to 2008, she was a Research Fellow with the Department of Electronics, Politecnico di Torino. From 2009 to 2012, she was the Head of the Antenna and EMC Laboratory, Istituto Superiore Mario Boella, Torino. Since 2012, she has been an Assistant Professor with the Department of Electronics and Telecommunications, Politecnico di Torino, where she has been an Associate Professor since 2014 and a Full Professor since 2021. Her main research activities concern numerical techniques based on integral equations and method of moments, with a focus on multiresolution and hierarchical schemes, domain decomposition, preconditioning and fast solution methods, advanced quadrature integration schemes, and analysis of glide-periodic structures. Moreover, her research interests include the modeling, design, realization and testing of microwave imaging and sensing systems for medical and industrial applications. She received the Lot Shafai Mid-Career Distinguished Award from the IEEE Antennas and Propagation Society (AP-S) in 2017, the Best Paper Award at the Spanish URSI Symposium in 2023, and the Best Electromagnetics Paper Award at the 20th European Conference on Antennas and Propagation (EuCAP) in 2026. She was an Associate Editor of the IEEE Transactions on Antennas and Propagation (2018-2024) and the founder and responsible of the Women in Engineering Column in the IEEE Antennas and Propagation Magazine (2019-2024). She is a member of the EurAAP Board of Directors and the Vice-Chair of the IEEE AP-S Expanding Collaboration & Engagement (ECE) committee.

This work is licensed under a Creative Commons Attribution-NonCommercial-NoDerivatives 4.0 License.
For more information, see https://creativecommons.org/licenses/by-nc-nd/4.0/